Charles University
Faculty of Science

Study program: Inorganic Chemistry

Mgr. Barbora Pitňa Lásková

Electrochemical, photoelectrochemical and spectroelectrochemical characterization of nanomaterials

Elektrochemická, fotoelektrochemická a spektroelektrochemická charakterizace nanomateriálů

Doctoral thesis

Supervisor: Prof. RNDr. Ladislav Kavan, DSc.
Supervisor-consultant: RNDr. Markéta Zukalová, Ph. D.

Prague, 2017

Acknowledgements

First of all I would like to express my sincere thanks to my supervisor, Prof. Ladislav Kavan, for giving me the opportunity to become a member of his research group and to complete my thesis at J. Heyrovský Institute of Physical Chemistry of the CAS. I am grateful for his kind support, inspiring advices, motivating guidance and for his invaluable help during the whole study.

I would like to thank to my consultant Dr. Markéta Zukalová who was always ready to discuss my ideas and to give me advice in any experimental problems.

I would like to express my thanks also to Prof. Michael Grätzel and his colleagues in Lausanne where I spent six months full of rewarding experience. Special thanks to Dr. Thomas Möehl for great cooperation and for many helpful suggestions in the field of electrochemical impedance spectroscopy.

My special thanks also to all the co-authors of submitted publications, whose work and help was essential for the thesis to be finished.

I am grateful to my colleagues at Department of electrochemical materials Dr. Otakar Frank, Mgr. Milan Bouša and to all others for their priceless help, outstanding cooperation and for inspiring, relaxed atmosphere at work.

Finally, I would like to thank my husband Alex, my daughter Viktorie, my parents and my sister for their encouragement, support during my Ph.D. studies and also for their great patience during the writing of this thesis taking sometimes too long.

Prohlášení

Prohlašuji, že jsem závěrečnou práci zpracovala samostatně a že jsem uvedla všechny použité informační zdroje a literaturu. Tato práce ani její podstatná část nebyla předložena k získání jiného nebo stejného akademického titulu.

V Praze dne 10.7.2017

Mgr. Barbora Pitňa Lásková

Prohlášení spoluautorů

Jménem svým i ostatních spoluautorů prohlašuji, že podíl Barbory Pitňa Láskové na společných publikacích je minimálně roven alikvotnímu podílu připadajícímu na každého z autorů.

V Praze dne 27.6.2017

Prof. RNDr. Ladislav Kavan, DSc.

Prohlášení spoluautorů

Jménem svým i ostatních spoluautorů prohlašuji, že podíl Barbory Pitňa Láskové na společných publikacích je minimálně roven alikvotnímu podílu připadajícímu na každého z autorů.

V Praze dne 26.6.2017

RNDr. Markéta Zukalová, Ph. D.

The work presented in this thesis was financially supported by the Czech Academy of Sciences (contract IAA 400400804 and KAN 200100801), the Grant Agency of the Czech Republic (contracts No. 13-07724S, P108/12/0814 and 15-06511S), the Sciex-NMSch programme (project 12.376) and the Czech Ministry of Education, Youth and Sports (COST Action CM1104, contract No. LD13060, contract no. LC-510, contract No. LM2015087)

Abstract

Titanium dioxide (TiO_2) and spinel $Li_4Ti_5O_{12}$ belong to widely studied semiconducting metal oxides. Nanocrystalline TiO_2 and $Li_4Ti_5O_{12}$ are attractive materials for applications in Li-ion batteries and the former also for photoelectrochemical solar cells. Moreover, spinel $Li_4Ti_5O_{12}$ could be a promising material for Na-ion batteries too, because of possible accommodation of larger Na^+ ions (compared to Li^+). The nanocrystalline TiO_2 anatase with a predominant {001} facet was studied electrochemically by cyclic voltammetry of Li^+ insertion and by chronoamperometry and compared with anatase materials with dominating {101} facet. Both voltammetric and chronoamperometric diffusion coefficients and activation energies proved higher activity of anatase {001} nanosheets toward Li^+ insertion than that of the usual anatase nanoparticles exposing the {101} facet. Subsequently, the flatband potential and electron kinetics of TiO_2 anatase nanocrystals with mostly exposed facet {101} or {001} were compared. The anatase {001} nanoplatelets exhibited more negative flatband potential, higher chemical capacitance and longer electron lifetime than anatase {101} nanoparticles. The Li^+ insertion into TiO_2 anatase nanoparticles was studied by Raman spectroscopy and by in situ Raman spectroelectrochemistry. Four combinations of isotopologues, namely $^{6/7}Li_xTi^{16/18}O_2$ (x is the insertion coefficient), were prepared and studied. The combination of experimental and theoretical Raman frequencies with the corresponding isotopic shifts brings new inputs for still open questions about the Li-insertion into TiO_2 (anatase). The cyclic voltammograms of Li^+ insertion into TiO_2 (B) and anatase provided information about capacitive contributions to the overall charge of Li-storage. The enhancement by 30% is found in capacitive charges (normalized to the total voltammetric charges) in TiO_2 (B) compared to those in anatase. Facilitated Li-insertion in TiO_2 (B) is explained by different charging mechanism caused by pseudocapacitive Li-storage in the bulk TiO_2 (B). Sodium insertion into nanocrystalline spinel, $Li_4Ti_5O_{12}$ (nanoLTS) was investigated by cyclic voltammetry. Changes in the cyclic voltammograms of nanoLTS were observed during long-term cycling. Raman spectroscopy of nanoLTS after Na-insertion reveals a formation of orthorhombic $Li_{0.5}TiO_2$ phase. The occurrence of this phase is ascribed to induced Li^+ redistribution into trace anatase impurities.

Keywords: titanium dioxide, TiO_2 (B), anatase {001}, $Li_4Ti_5O_{12}$, lithium insertion, spectroelectrochemistry

Abstrakt

Oxid titaničitý (TiO_2) a spinel $Li_4Ti_5O_{12}$ patří mezi široce studované polovodivé oxidy kovů. Nanokrystalické formy TiO_2 a $Li_4Ti_5O_{12}$ jsou atraktivní pro použití v lithiových bateriích a oxid titaničitý také pro fotoelektrochemické solární články. Spinel $Li_4Ti_5O_{12}$ by díky své struktuře umožňující ukládat větší Na^+ ionty (v porovnání s Li^+ ionty) mohl být i slibným materiálem pro sodíkové baterie. Nanokrystalický TiO_2 anatas s převládající plochou {001} byl studován elektrochemicky cyklickou voltametrií inserce lithia a chronoamperometrií a porovnán s referenčním anatasem s dominantní plochou {101}. Voltametrické a chronoamperometrické difusní koeficienty a aktivační energie prokázaly, že anatasové nanokrystaly {001}mají oproti standardním anatasovým nanočásticím vyšší aktivitu vůči inserci Li^+. Anatasové nanokrystaly TiO_2 s nejvíce exponovanou plochou {101} byly následně porovnávány s nanokrystaly s dominantní plochou {001} z hlediska potenciálu rovných pásů a kinetiky elektronů. Anatasové nanodestičky {001} měly ve srovnání s anatasovými nanočásticemi {101} negativnější potenciál rovných pásů, vyšší chemickou kapacitu a delší dobu života elektronů. Ramanovou spektroskopií a in situ Ramanovou spektroelektrochemií byla studována inserce Li^+ do TiO_2 anatasových nanočástic. Byly připraveny a studovány čtyři izotopologické kombinace, $^{6/7}Li_xTi^{16/18}O_2$ (kde x je inserční koeficient). Kombinace experimentálních a teoretických Ramanových frekvencí s odpovídajícími izotopickými posuny představuje nový přístup k řešení otevřených otázek inserce lithia do TiO_2 (anatasu). Cyklické voltamogramy inserce lithia do TiO_2 (B) a anatasu poskytly informaci o podílu kapacitního příspěvku k celkovému náboji uloženého lithia. Bylo zjištěno 30%ní navýšení kapacitního příspěvku (normalizovaného na celkový uložený náboj) v TiO_2 (B) oproti kapacitnímu příspěvku v anatasu. Usnadněnou inserci Li^+ do TiO_2 (B) lze vysvětlit odlišným mechanismem ukládání Li^+ do TiO_2 (B), které je pseudokapacitní. Cyklickou voltametrií byla studována inserce sodíku do nanokrystalického spinelu, $Li_4Ti_5O_{12}$ (nanoLTS). Během dlouhodobého cyklování byly pozorovány změny v cyklickém voltamogramu nanoLTS. Ramanova spektra nanoLTS po inserci Na ukázala, že dochází ke zformování kosočtverečné fáze $Li_{0.5}TiO_2$ v nanoLTS. Vznik této fáze je zdůvodňován indukovanou redistribucí Li^+ iontů do stopových anatasových nečistot.

Klíčová slova: oxid titaničitý, TiO_2 (B), anatas {001}, $Li_4Ti_5O_{12}$, inserce lithia, spektroelektrochemie

Table of Contents

1. Introduction

1.1 Titanium dioxide

Titanium is the ninth most abundant element in the earth's crust representing approximately 0.6 percent by mass. Titanium is not found as a pure metal in nature due to its strong affinity for oxygen, carbon and nitrogen, making difficult to obtain it in the pure state. Its important minerals are ilmenite ($FeTiO_3$) and rutile (TiO_2). TiO_2, titanium dioxide was discovered in 1791 and its commercial production started in the 1920s.[1] About 95% of titanium ore is processed into titanium dioxide, which is the most widely used titanium product.[2] Two manufacturing methods are usually used in industry to produce TiO_2. The first one is the sulfate process, where raw material, $FeTiO_3$ ilmenite, is treated with sulfuric acid. The final products of this method are two forms of TiO_2, rutile and anatase. The second method is the chlorine process based on application of chlorine on rutile ore. Today chlorine process is favored mainly due to high purity of final product and economic reasons.

Titanium dioxide is an important low cost, chemically stable, nontoxic oxide material with a wide range of applications. TiO_2 is utilized mainly as a white pigment in paints because of its high refractive index and sufficiently small particle size which lead to effective light scattering over a wide range of wavelengths. Next well-known optical applications of titanium dioxide are in cosmetic industry as an ultra-violet absorber or the use in anti-reflection coatings. The optical, chemical and electronic properties predetermined TiO_2 also for applications in self-cleaning surfaces, food additives, corrosion-resistant coatings, anti-fogging coatings and sensor devices. TiO_2 nanoparticles illuminated by UV light have high redox activity, therefore they can be employed as heterogeneous photocatalysts for degradation of organic pollutants in different environments such as water or air. In addition TiO_2 has been extensively studied as photoanode in photoelectrochemical solar cells, namely in dye-sensitized solar cells (DSSCs). The next significant property of titanium dioxide is its ability to accommodate Li^+, which classifies it as a candidate for anodes in rechargeable Li-ion batteries. The attractiveness of TiO_2 anode for this type of batteries is further supported by its cycling stability at high charging rates, reasonable capacity and enhanced safety compared to that of graphite anode because of higher Li-insertion potential.

Titanium dioxide occurs in several natural and synthetic polymorphs. Tetragonal rutile (space group $P4_2/mnm$), tetragonal anatase ($I4_1/amd$) and orthorhombic brookite (*Pbca*) can be found in nature.[2, 3] The fourth more rare fundamental crystal form, monoclinic TiO_2 (B) (*C2/m*), was discovered in nature in 1991 by Banfield.[4] This mineral was revealed only in two geological localities in Switzerland.[3] Except of these forms, the high-pressure phases of TiO_2 with columbite (*Pbcn*) baddeleyite ($P2_1/c$), fluorite (*Fm3m*), pyrite (*Pa3*) and cotunnite (*Pnma*) structure are known.[2, 3] The most stable TiO_2 phase for macroscopic crystals is rutile, but the most thermodynamically stable polymorph for particle size below 10-20 nm is anatase and the thermal anatase-to-rutile transition for nanoparticles starts at temperatures over 500°C.[5-8] Therefore, the majority of TiO_2 applications are based on rutile and anatase forms due to their stability, easy production and properties. However, the metastable monoclinic TiO_2 (B) has currently attracted an attention of many research teams because of its structure promising for charge storage applications.[9-11] Brookite structure is not experimentally investigated as much as the others because brookite is a metastable phase with a complicated and low-symmetry structure and formation of brookite TiO_2 is almost always accompanied by the presence of secondary phases such as anatase and/or rutile.[12]

TiO_2 rutile

Rutile polymorph has a tetragonal symmetry and its unit cell contains two TiO_2 formula units with the Ti and O coordination numbers six and three, respectively ($a = b = 0.4584$ nm, $c = 0.2953$ nm)[3]. Rutile structure can be described in terms of chains of TiO_6 octahedra, where each Ti^{4+} ion is surrounded by an octahedron of six O^{2-} ions. The octahedrons show a slight orthorhombic distortion and each octahedron is in contact with 10 neighbor octahedrons (8 sharing corner oxygen atoms and 2 sharing edge oxygen pairs). [13] The rutile structure is shown in Figure 1. Anatase structure is based on analogous TiO_6 building blocks, but with different arrangement (see Fig 1), which leads to different mass densities and electronic band structures of these two forms of TiO_2. Rutile has more compact structure, higher thermal stability (melting point at 1825 °C) and higher refractive index compared to anatase.[2, 14] Therefore the rutile form is generally preferred in optical applications. Rutile is used in pigments, anti-reflection coatings, as UV absorber for cosmetics and plastics, transparent UV absorbers for food packaging and

besides that in corrosion protection coatings and electroceramics. Rutile with refractive index 2.9 gives a high sun protection factor in sunscreens and it is preferred in sunscreens more than anatase, since the latter inadequately more strongly adheres on skin.[2, 15]

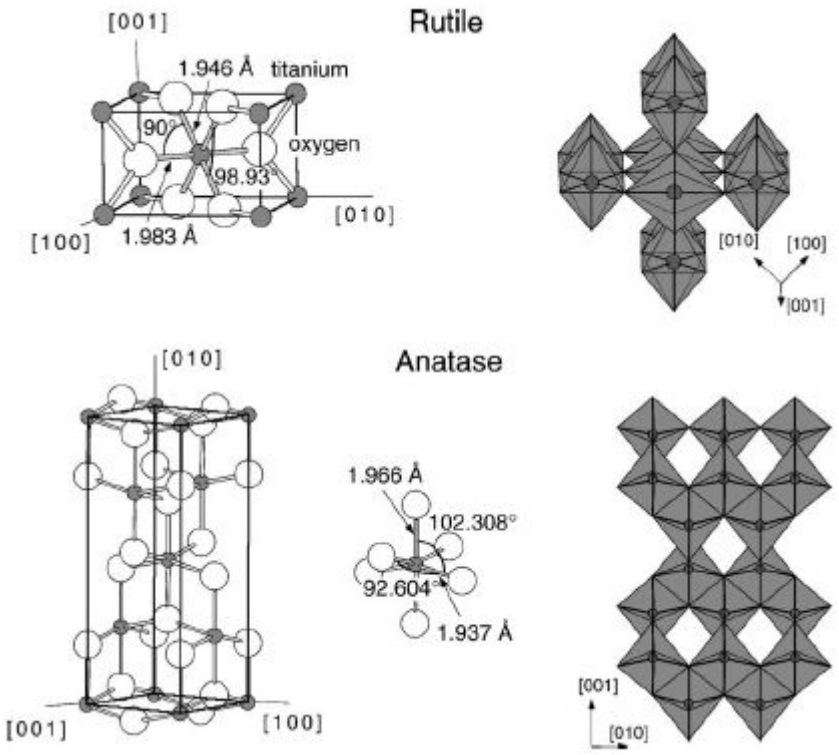

Figure 1. Structures of rutile and anatase with positions of Ti and O atoms on the left. The corresponding TiO_6 octahedra arrangements are shown on the right side. Reprinted with permission from Ref.[16]. Copyright (2003) Elsevier.

TiO_2 anatase

Tetragonal unit cell of anatase contains four TiO_2 units with the Ti and O coordination numbers six and three, respectively ($a = b = 0.3733$ nm, $c = 0.937$ nm)[3]. Anatase structure can be described by chains of TiO_6 octahedra as in the case of rutile, but octahedron is more distorted in anatase (see Fig. 1). The Ti-Ti distances are larger in anatase, whereas the Ti-O distances are

shorter than those in rutile. In anatase structure each octahedron is in contact with eight neighbors (four sharing an edge and four sharing a corner).[13] The anatase form has more open structure, higher electron mobility and higher photocatalytic activity compared to rutile, which favors use of this modification in Li-ion batteries, DSSCs, electrochromic windows and photocatalysts.

Typical anatase nanocrystals have a shape of truncated bipyramids with dominating facet {101}, which represents more than 94% of the total crystal surface area. Remaining facet on anatase crystal is {001} (see Figure 2).[17] The domination of {101} facet is rationalized by its lowest surface energy. Only rarely rhombic-shaped crystals exposing {010} and {111} facets are found. The {001} and {010} facets show interesting activity in catalysis and photocatalysis and are called „reactive“ ones.[17-19] In 2008 Yang et al. discovered the synthesis of micrometer-sized platelets of anatase with high percentage (47%) of {001} facets, where the hydrothermal treatment in hydrofluoric acid (HF) is a morphology directing procedure.[20] Subsequently, studies reporting on polycrystalline materials enriched with up to 90% of the {001} facet followed.[21-23] The facile preparation of anatase crystals with predominant facet {001} led to deeper investigation of orientation-dependent effects in nanocrystalline anatase materials, which provided promising inputs for photocatalysis[24] and Li-ion batteries[17].

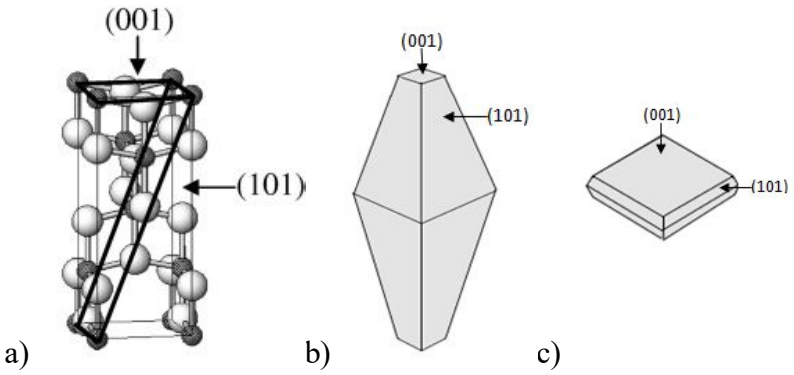

Figure 2. a) Anatase unit cell with {101} and {001} facets indicated. Adapted with permission from Ref.[25]. Copyright (2006) American Chemical Society. b) The shape of ordinary anatase crystal. c) The shape of anatase nanoparticle with predominant orientation {001}.

TiO_2 (B)

TiO_2 (B) has a monoclinic unit cell isotypic to that of Na_xTiO_2 ($x \cong 0.2$) with a = 1.2127 nm, b = 0.37537 nm, c = 0.6535 nm and β = 107.16 °.[26] It was first synthesized in 1980 by Marchand et al.[27] TiO_2 (B) structure is illustrated in Figure 3. It is characterized by two edge-sharing TiO_6 octahedra which are linked to the neighboring doublet of octahedra by corners.[3, 9, 28] Such an arrangement results in open channels along the b-axis in TiO_2 (B) fibrous structure. Low density of TiO_2 (B) compared to another TiO_2 modifications and presence of channels inside the structure has currently attracted attention of scientists because of facile Li^+ distribution in material through the channels and high Li-insertion coefficient, which make TiO_2 (B) attractive for Li-ion batteries.[9, 26, 29, 30]

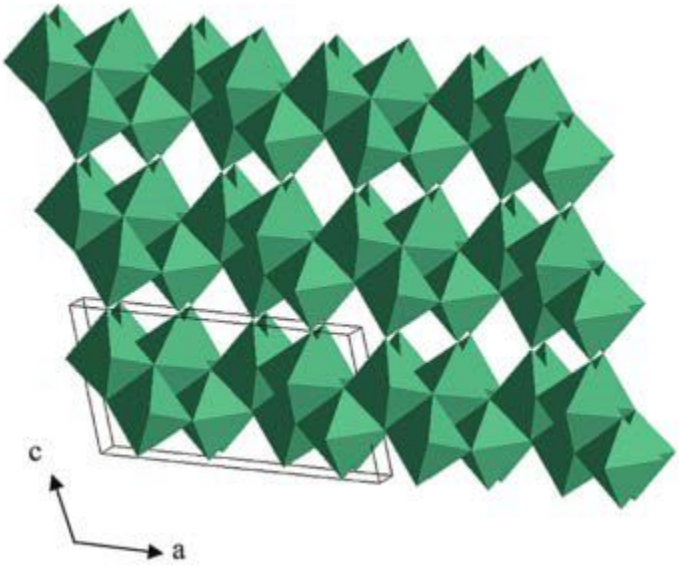

Figure 3. Structure of bulk TiO_2 (B) crystal represented by ribbons of edge-sharing TiO_6 octahedra, which are connected in the c direction by corner-sharing. Black lines correspond to unit cell. Adapted with permission from Ref.[31]. Copyright (2009) American Chemical Society.

Electronic properties of TiO_2

Electronic structure of titanium dioxide is more complex[13], but in a simplified way 3d and 4s valence electrons of titanium interact with 2p orbitals of oxygen. Therefore, the edge of TiO_2 valence band basically matches with occupied O 2p orbitals and the conduction band edge corresponds mainly to the empty Ti 3p orbitals. Conduction band and valence band edges are separated by a gap of about 3 eV, hence titanium dioxide belongs to wide bandgap semiconductors. More precisely, the bandgap energy of TiO_2 is 3 eV, 3.2 eV and 3-3.2 eV for rutile, anatase and TiO_2 (B), respectively.[3, 14, 28]

Conductivity of intrinsic semiconductor is based on a movement of the same concentration of electrons and holes and the Fermi level is located in the middle of bandgap. However, the position of Fermi level in material can be changed by defects in structure or by impurities in material. Semiconductor with electrons as major charge carriers has Fermi level shifted towards the conduction band and it is called *n*-type semiconductor. In each TiO_2 material, natural or synthesized, defects are always present. The defects are Ti^{3+} and oxygen vacancies, which cause introducing of extra electrons into the conduction band.[14] Therefore, the real formula of titanium dioxide is TiO_{2-x} ($x \approx 0.01$) [3, 28] and it is an *n*-type semiconductor.

TiO_2 electrodes immersed in liquid electrolyte solutions behave according to the same rules as all the other *n*-type semiconductors. If the Fermi level of a semiconductor and the redox potential of a solution are different, the electron redistribution at the interface electrode/electrolyte solution starts to establish an equilibrium. This results in a bending of the conduction and valence bands of a semiconductor. In the case of electrode's Fermi level higher than redox potential of solution, there is a positive charge in electrode space charge region, which leads to upward bending of band edges. Since the major charge carriers are transferred from this region, it is called depletion layer.[14] If the Fermi level of semiconductor is equal to energy of redox potential of electrolyte no band bending occurs and this potential is referred to as *flatband potential,* E_{fb}. At potentials more negative than flatband potential the electrons are concentrated at space charge regime, the bands are bended downward and the accumulation layer is created. The accumulation layer in TiO_2 electrode can be compensated by insertion of small

positive ions into a lattice of semiconductor material. This situation is described in details in the next chapter.

1.1.1 Lithium insertion into TiO_2

An injection of negative charge into TiO_2 electrode (for example electrons from back contact) can be compensated by adsorption of positive ions from electrolyte solution or by insertion of small positive ions into material of electrode. The inserted ions have to be small enough to fit into cavities in the host lattice. Li^+ or Na^+ are two examples. Insertion of Li^+ into TiO_2 has been intensively studied during last decades due to its applicability in Li-ion batteries. The electrochemical accommodation of lithium in TiO_2 anatase can be described as follows:

$$TiO_2 + x(Li^+ + e^-) \rightarrow Li_xTiO_2 \quad (x \approx 0.5) \qquad (1)$$

During lithiation tetragonal anatase transforms reversibly to orthorhombic lithium titanate $Li_{0.5}TiO_2$ (space group *Imma*). Unit cell dimensions of $Li_{0.5}TiO_2$ are a = 0.3819 nm, b = 0.4084 nm, c = 0.9066 nm.[32] These two phases, tetragonal one with anatase structure and orthorhombic lithium titanate, coexist in electrode at first stages of lithiation. Ren et al. reported that the orthorhombic phase exists already at an insertion coefficient 0.05.[33] The Li-insertion coefficient x is usually close to 0.5 for anatase, but reversible capacities of $x \approx 0.8$ were also reported in certain anatase nanostructures.[34-36] Tetragonal structure of $LiTiO_2$ was observed too, although only for anatase nanocrystals of 7 nm in size or smaller and its detection is not always straightforward.[33, 37] The Li^+ insertion into rutile is crystal-size depend and the Li^+ capacity is reasonably higher for nanometer sized rutile crystals compared to micro-sized one. The Li - insertion coefficient for nanocrystalline rutile is typically 0.1- 0.5. Wagemaker et al. reported about the monoclinic structure of Li_xTiO_2 ($x \approx 0.53$) evolved in rutile and the transformation to another monoclinic structure during further lithiation up to 0.85.[38] However, the Li^+ diffusion is presumably slower for rutile due to more compact structure of rutile compared to anatase.[39] Similar or larger insertion coefficients were observed for TiO_2 (B). Optimization of TiO_2 (B) synthesis increases its capacity (x up to 0.91) and accelerates charging. [40-42]

1.1.2 TiO_2 in dye-sensitized solar cells

Dye-sensitized solar cell (DSSC), also called Grätzel cell, is an attractive alternative of solid state photovoltaics due to efficiency, low cost and easy fabrication. The basic construction of DSSC is illustrated in Figure 4. The photoanode consists of TiO_2 film deposited on fluorine-doped tin oxide (FTO) glass and specially designed dye adsorbed on TiO_2 nanoparticles surface. The cathode is platinum or carbon on FTO glass support. Both electrodes communicate through electrolyte solution with suitable redox couple e.g. iodide/triiodide. Principle of DSSC is a photoexcitation of electrons in dye by sunlight, injection of the exited e^- into TiO_2 conduction band and subsequent collection on the back contact. Afterwards the oxidized dye is regenerated by electrons from electrolyte solution which acquire e^- from cathode. Real system is more complex and various additional factors as recombination play role. A detailed description of all DSSCs aspects is possible to find in excellent textbook on this topic.[43] Optimization of DSSC has been a subject of numerous studies. Nanocrystaline TiO_2 anatase was found to be the best material for this device and promising data were acquired also by replacing the traditional electrolyte solution redox relay (I_3^-/I^-) by other systems.

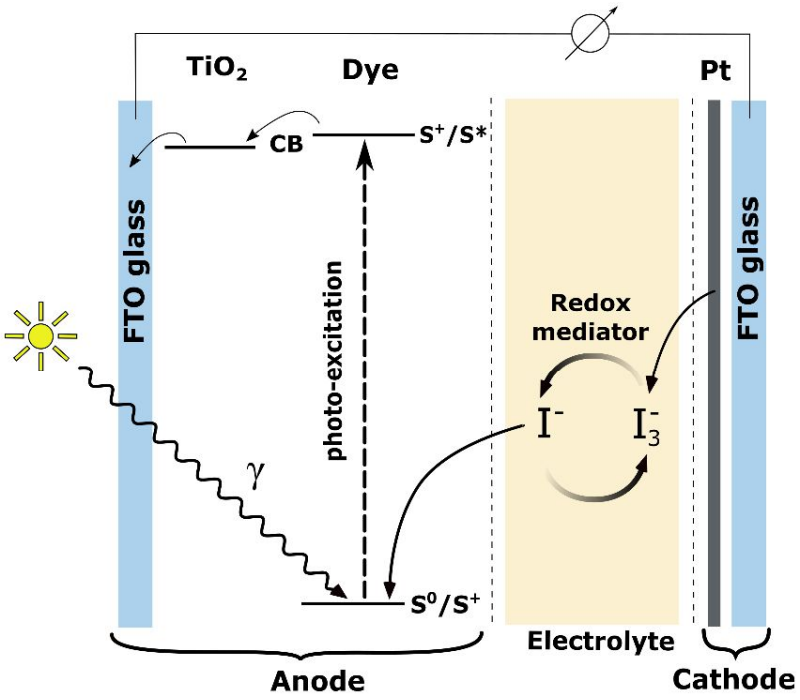

Figure 4. Scheme of assembling and principle of dye-sensitized solar cell.

TiO_2 anatase works as an electron collector in a new photovoltaic system, perovskite solar cells, too. This novel type of solar cells has been intensively studied during last few years. These cells are based on metal halide perovskite materials, such as methylammonium lead triiodide. Briefly, a compact TiO_2 layer is deposited on FTO glass. Sometimes, an additional mesoporous TiO_2 layer is used on top of the compact layer and plays a role of a scaffold for a photo-active perovskite layer, which is deposited on top of the TiO_2 porous film, but this film is not mandatory. Main advantage of perovskite cells is their high solar conversion efficiency, however, a toxicity of the principal component and a long term stability are fundamental issues to be solved in nowadays studies of these devices.[44, 45]

1.2 Spinel $Li_4Ti_5O_{12}$

Spinel $Li_{4/3}Ti_{5/3}O_4$ ($Li_4Ti_5O_{12}$) is a semiconductor with cubic lattice (space group *Fd3m*).[28] It accommodates Li^+ according to the equation (2):

$$Li_4Ti_5O_{12} + 3e^- + 3Li^+ \leftrightarrow Li_7Ti_5O_{12} \quad (2)$$

The Li^+ accommodation occurs without significant changes of spinel lattice constants and the material exhibits great stability during cycling. Hence, the lithium titanate spinel $Li_4Ti_5O_{12}$ is an interesting material for negative electrodes in Li-ion batteries.[28]

Spinel $Li_4Ti_5O_{12}$ should be a promising material for Na-ion batteries too. Ion radius of Na (1.02 Å) is larger than that of Li (0.76 Å), hence, Na^+ accommodation occurs only for host materials with large interlayer spacing.[46] Kitta et al.[47] found that during Na^+ insertion into pure $Li_4Ti_5O_{12}$ an Na-substituted lithium titanate spinel phase is generated and co-exists with $Li_4Ti_5O_{12}$ in a single particle.[46]

$$(Li_3)(LiTi_5)(O_{12}) + xNa^+ \rightarrow (Na_xLi_{3-x})(LiTi_5)(O_{12}) + xLi^+ \ (0 < x < 3) \quad (3)$$

Sun et al.[48] predicted even three-phase separation mechanism. However, the mechanism of Na-substituted lithium titanate spinel formation and its behavior upon cycling remain still unclear.

2. Aims of the thesis

This thesis is based on papers which are attached at the end of this text as **Appendices 1-7**.[17-19, 26, 29, 32, 46] These publications make an integral part of the thesis and the text below is an extended summary of the attached papers. The research is focused on investigation of nanomaterials attractive for applications in lithium-ion batteries and dye-sensitized solar cells. The subject follows previous studies of Prof. Kavan's group (Department of electrochemical materials, J. Heyrovsky Institute of Physical Chemistry of the CAS) on nanomaterials, especially on TiO_2 anatase and TiO_2 (B). Fundamental differences in Li^+ insertion behavior were observed for different exposed facets of anatase single crystals in the past. This motivated the aim of the thesis: comparison of the Li^+ insertion and intrinsic properties of anatase nanocrystals with different predominant facets {001} or {101} by electrochemical and photoelectrochemical methods. Namely by cyclic voltammetry, chronoamperometry, UV-Vis spectroelectrochemistry and electrochemical impedance spectroscopy of DSSCs employing anatase nanosheets or common anatase nanoparticles as photoanodes. Lithium insertion studies are additionally extended about a part focused on differences in charging mechanisms of TiO_2 anatase and TiO_2 (B). The aim of this part is to clarify previously observed differences in electrochemical response of both materials. The thesis is further concentrated on detailed investigation of structural changes in TiO_2 materials during lithium insertion. These changes are studied by in situ Raman spectroelectrochemistry, where isotope labeled compounds were used in one part of the research. The reason for Raman investigation was mainly an effort to assign all Raman peaks of the orthorhombic Li_xTiO_2 structure observed during Li^+ insertion into anatase tetragonal structure. In addition, Raman spectroscopy studies are accompanied by tracking of structural changes in lithium titanate spinel after Na^+ insertion, which aimed to explain changes in $Li_4Ti_5O_{12}$ material observed during Na^+ insertion/extraction cycling.

3. Experimental section

3.1 Materials

TiO_2 Anatase

Comparative studies of anatase {101} and anatase with predominant facet {001}

The anatase {001} was prepared by addition of 0.8-1.2 mL of hydrofluoric acid (HF) (≈50%) into 10 mL of titanium(IV) butoxide. The mixture was heated at 180-200 °C for 24 h in a Teflon cell encased in a stainless steel autoclave. Subsequently, the sample was collected, washed by Milli-Q water and dried at 100 °C. Four types of reference materials of anatase {101} were used. First reference material was prepared by the same way as anatase {001} nanosheets, but HF was replaced by the same amount of water. Second reference material was nanocrystaline anatase synthesized by hydrolysis of titanium(IV)-isopropoxide and hydrothermal recrystallization at 250 °C. Third comparative material was nanocrystalline anatase coded as C240. The C240 is characterized by particles of 10-20 nm in size and Brunauer−Emmett−Teller (BET) surface area of 89 m^2/g. It is prepared by hydrolysis of titanium tetra(isopropoxide) and hydrothermal recrystallization at 240 °C in autoclave. Fourth material with anatase {101} nanocrystals was P90 (from Degussa AG, Germany). It is a mixture of rutile, anatase (with >90% of anatase) and very small amount of TiO_2 (B). The surface area of P90 is S_{BET} =100 m^2/g. These materials were used in comparative studies of anatase {101} and anatase {001} properties, for more specific details please see **Appendices 1**[17]**, 6**[18] **and 7**[19]. The reference materials C240 and P90 were employed in other TiO_2 investigations as well (see **Appendices 2**[26]**, 4**[29]**, 5**[46]).

Raman spectroelectrochemistry of isotope labeled $Ti^{16/18}O_2$ anatase

The synthesis of TiO_2 samples was carried out in a vacuum apparatus. Vacuum distilled titanium tetrachloride (99.98% Aldrich) was hydrolyzed with $H_2{}^{18}O$ (Aldrich ^{18}O 99%) or H_2O with natural isotope composition. The product was heat-treated in vacuum at 450 °C to obtain anatase. Surface area of the product S_{BET} was 31 m^2/g for both O-isotopologues. These materials were used in Raman spectroelectrochemical investigation of lithium insertion into titanium dioxide using $^{16/18}O$ and $^{6/7}Li$ isotope labeling. For details please see **Appendix 3**[32].

TiO_2 (B) materials

Three TiO_2 (B) materials were used in this thesis. The first one (denoted as TBa) is a phase pure TiO_2 (B) synthesized by a method, which previously reported Zukalova et al.[9] This procedure is based on mixing of 10 g of amorphous TiO_2 with 7.8 g of Cs_2CO_3. The powder was then calcined at 800 °C for 4 h, mortared again, and reheated to 800 °C for 48 h to form cesium titanate. This product was subsequently vigorously stirred in excess of 1 M HCl for 4x24 h, while hydrochloric acid solution was replaced every 24 h by new one. The product was finally dried in air. Its BET surface area was S_{BET} = 28 m^2/g. For more details please see **Appendix 2**[26] **and 4**[29]. In the Raman spectroelectrochemical studies (**Appendix 4**[29]) the second TiO_2 (B) material (Lor-035-013B, calcined for 7 h at 400 °C; SusTech GmbH & Co. Kg, Darmstadt, Germany) was used (denoted as TBb). Its synthesis was described elsewere.[49] The third TiO_2 (B) material was also obtained from SusTech GmbH & Co. Kg, Darmstadt, Germany. It was prepared by dissolving of 8 mL $TiCl_4$ in 20 mL of H_2O and 10 M NaOH was added to a total volume of 150 mL. The mixture was autoclaved at 250 °C for 6 h. Subsequently, the material was washed with hydrochloric acid and water and further autoclaved in water or weak acidic solvents for several hours. This material (denoted as N21) consists of 49% of TiO_2 (B) and 51% of anatase (see **Appendix 2**[26]).

Rutile

In Raman spectroelectrochemical studies (**Appendix 4**[29]) a commercial powder of TiO_2 rutile PK5556 (Bayer, Germany) was used. It is a nanocrystalline material with S_{BET} = 103 m^2/g which was calcined for 20 min at 800 °C.

$Li_4Ti_5O_{12}$

$Li_4Ti_5O_{12}$ nanocrystalline spinel (nanoLTS) was synthesized according to previously published procedure.[50, 51] Briefly: 1.34 M solution of lithium methoxide (LiOMe, Aldrich) in absolute ethanol was mixed with a stoichiometric amount (4/5) of titanium(IV) isopropoxide (Aldrich) or titanium(IV) n-butoxide, (Aldrich). The solution was hydrolyzed and concentrated on rotary evaporator (40 °C, 20 mbar) to a concentration of 10–20 wt%. Polyethylene glycol (molecular weight 20 000, Merck) was added in the proportion of 100-150% of the weight of

$Li_4Ti_5O_{12}$, and the mixture was stirred overnight. The resulting slurry was then calcined at 500 °C 1 hour. Reference LTS material was purchased from Aldrich (Aldrich LTS). See **Appendix 5**[46]

Lithium perchlorate

In Raman spectroelectrochemical investigation of lithium insertion into titanium dioxide using $^{16/18}O$ and $^{6/7}Li$ isotope labeling lithium-isotope labeled salt $^{6}LiClO_4$ (with 95 atom % of ^{6}Li, Sigma Aldrich) was used as an electrolyte. A common lithium perchlorate (Sigma Aldrich) approximated as $^{7}LiClO_4$ (natural abundance of ^{7}Li is 92.5%) was used for comparison. For details please see **Appendix 3**[32].

3.2 Preparation of electrodes

Electrodes for Li/Na insertion studies in a glove box were prepared as follows: The powder samples were sonicated in ethanol. Titanium grid (5 mm x 20-25 mm, Goodfellow or Dexmet) was used as an electrode support. The electrodes were prepared by dip-coating and the coated area was 5 mm x 10 mm. The electrodes were dried in air and then sintered at 450 °C for 30 min. The final mass of active material for Li insertion was between 0.1 and 0.7 mg (see **Appendix 1**[17]**, 2**[26]). Blank experiment with Ti-grids annealed at the same conditions proved a negligible electrochemical charge capacity of the Ti grid compared to that of the active material.

Electrodes for Raman spectroelectrochemical studies were prepared as follows: Powder titania samples were dispersed in an aqueous medium into a viscous paste. The powders were mixed with 4% aqueous solution of hydroxypropylcellulose (Aldrich, MW 100 000) and with 10% solution of Triton-X100 (Fluka) after which H_2O was added. Platinum mesh (4 mm x 4 mm, Goodfellow) served as a conductive support and a TiO_2 film was deposited by dip-coating. The coated area was approximately 2 mm x 4 mm. All prepared electrodes were dried in air and subsequently calcined in air at 450 °C for 30 min. More details in **Appendix 3**[32]**, 4**[29].

Electrodes for flatband potential studies were fabricated from all parent powder materials using either aqueous paste or simply ethanolic suspension. The aqueous paste was prepared by process similar to procedure described in the previous paragraph apart from 10% aqueous

solution of acetylacetone which was added. The obtained slurry was deposited on F-doped SnO_2 (FTO) glass with Kapton foil tape defining the TiO_2 film edges. Ethanolic films were prepared by sonication of powder samples in ethanol and deposition of the ethanolic suspension on FTO glass by doctor blading method. All films were then calcined in air at 450 °C for 30 min. More details in **Appendix 6**[18].

3.3 Solar cells fabrication

*Solar cells for voltage enhancement measurement*s consisted of TiO_2 films made from aqueous or ethanolic suspensions as described in the last paragraph of previous section. It was sensitized by a C101 dye [NaRu(4,4‘-bis(5-hexylthiophene-2-yl)-2.2‘-bipyridine)(4-carboxylic acid-4‘-carbxylate-2,2‘-bipyridine)$(NCS)_2$] with chenodeoxycholic acid as a coadsorbent. The details of sensitization conditions are described in **Appendix 6**[18]. The solar cell was subsequently assembled with platinized FTO counter electrode using a Surlyn tape (25 µm in thickness) as a seal and spacer. The electrolyte solution was 0.6 M *N*-metyl-*N*-butyl imidazolium iodide, 40 mM I_2, 0.075 M lithium iodide, 0.26 M *tert*-butylpyridine and 0.05 M guanidine thiocyanate in acetonitrile/valeronitrile (85/15 %, *v/v*). The cell active area was defined by a mask to 0.22 cm^2.

Solar cells for electron kinetics investigations were composed from TiO_2 anatase {101} or {001} photoanode sensitized by an organic dye D35, [(E)-3-(5-(4-(Bis(2’,4’-dibutoxybiphenyl-4-yl)amino)phenyl) thiophen-2-yl)-2-cyanoacrylic acid]. The TiO_2 anatase films for photoanodes were prepared by usual procedure for DSSC photoanode preparation. The anatase powders were transformed to paste according to previously reported procedure[52] and then screen printed on FTO glass covered by TiO_2 blocking layer. The resulting films were calcined at 500 °C for 30 min and after cooling were post-treated in 1 mL of 2 M $TiCl_4$ aqueous solution with 150 mL of H_2O for 20 min at 75 °C for dye-loading improvement. A thickness of all anatase {101} or {001} films prepared by this way was 3.45 ± 0.25 µm. The DSSC was assembled after photoanode sensitization. The Surlyn tape (25 µm in thickness) play role of a seal and spacer between anatase photoanode and platinized FTO counter electrode. Two types of electrolyte solution were used: the iodine-based electrolyte solution Z946 (see **Appendix 7**[19] or Ref. [53]) and the cobalt-based electrolyte solution which was composed as follows: 0.1 M bis(trifluoromethane) sulfonimide (TFSI) lithium salt, 0.5 M nonylpyridine, 0.25 M

$[Co^{II}(bpy)_3](TFSI)_2$ (bpy = 2,2'-bipyridine) and 0.06 M $[Co^{III}(bpy)_3](TFSI)_3$. The active solar cell area for illumination was 0.28 cm^2. The detailed description of all assembling aspects is in **Appendix 7**[19].

3.4 Methods

BET surface areas of the materials were determined from nitrogen adsorption isotherms at 77 K using the Micromeritics ASAP 2020 instrument. *X-ray diffraction* (XRD) was investigated on powder sample by means of Bruker D8 Advance diffractometer using Cu Kα radiation. *Scanning electron microscopy* (SEM) images and *energy dispersive X-ray* (EDX) analyses were acquired at Hitachi FE SEM S-4800 microscope equipped with the Noran EDX system. *UV-Vis spectra* were collected by UV-vis-NIR spectrometer PerkinElmer Lambda 1050. *X-ray photoelectron spectroscopy (XPS) and ultraviolet photoelectron spectroscopy (UPS)* experiments were carried out using a Scienta ESCA 200 spectrometer in ultrahigh vacuum (ca.10^{-10} mbar) with an AlKα source and by the He lamp providing photon energies of 1486.6 eV and 21.22 eV, respectively (for UPS details see **Appendix 7**[19]).

Electrochemical measurements of Li insertion were carried out in one-compartment cell using an Autolab Pgstat -30 (Metrohm) controlled by GPES-4 software. The electrolyte solution was 1 M $LiN(CF_3SO_2)_2$ in ethylene carbonate (EC) and dimethyl carbonate (DMC) mixture (1:1), or in ethylene carbonate + 1,2-dimethoxyethane (1:1) alternatively. The reference and counter electrodes were from Li metal. These cells were kept in a glove box under argon atmosphere.

Electrochemical measurements of Na insertion were carried out in one-compartment cell using an Autolab Pgstat-302N (Metrohm) controlled by GPES-4 and Nova 2.1 software. The Na-insertion experiments were carried out in 1 M $NaPF_6$ + ethylene carbonate (EC)/diethylcarbonate (DEC) (1/1 by volume) in a glove box with an argon atmosphere. Reference and auxiliary electrodes were Na metal.

Raman spectroelectrochemical measurements were carried out in an airtight spectroelectrochemical cell under argon using a μAutolabIII (Metrohm Autolab) controlled by the NOVA 1.5 software. The spectroelectrochemical cell is illustrated in Figure 5a. An

electrolyte solution was 1 M $LiClO_4$ in EC/DMC (1/1 w/w). A counter electrode was from Pt metal and the AgCl-coated Ag wire was employed as an pseudoreference electrode. The latter is a convenient reference electrode for in situ Raman spectroelectrochemistry due to its easier use compared to commercial Ag/AgCl electrodes. To calibrate a potential of our Ag/AgCl-pseudoreference electrode, cyclic voltammograms of Li insertion were reproduced against the usual Li/Li^+ reference electrode in a glove box under Ar atmosphere (in 1 M $LiClO_4$).

Raman spectra were measured on a MicroRaman system (LabRAM HR spectrometer, Horiba Jobin–Yvon) with an Olympus BX microscope. The spectra were excited by a He–Ne laser, 633 nm. Raman spectrometer was calibrated before each set of measurements using the F_{1g} line of Si at 520.2 cm^{-1} as a reference.

Optical determination of the flatband potential of nanocrystalline anatase {101} and {001} was made by a spectroelectrochemical method described in Ref.[54-56]. The measurement was carried out in 0.2 M $NaClO_4$ (pH adjusted by $HClO_4$ or NaOH) using UV–vis–NIR spectrometer PerkinElmer Lambda 1050 interfaced to a potentiostat. Measurements were performed in transmission mode at gradually decreasing potentials from 0 V to −1.2 or −1.4 V. Potential was set, and after 1.5 min at the given potential, the spectrum was measured. The cell assembly is illustrated in Figure 5b. For data processing, the measured spectra were normalized by subtracting the spectrum measured at 0 V.

Electrochemical impedance spectroscopy (EIS) was performed with a BioLogic SP300 potentiostat on complete solar cells in the dark and under simulated solar illumination close to 1 sun (90 mW cm^{-2}). The applied bias potential was from 0 V to about open-circuit voltage (Voc) in 50 mV steps. A sinusoidal potential perturbation (20 mV amplitude) was applied over the bias potential. The resulting spectra were fitted to the transmission line model[57] with the Zview software (Scribner).

For more specific details about all used techniques please see particular appendices.

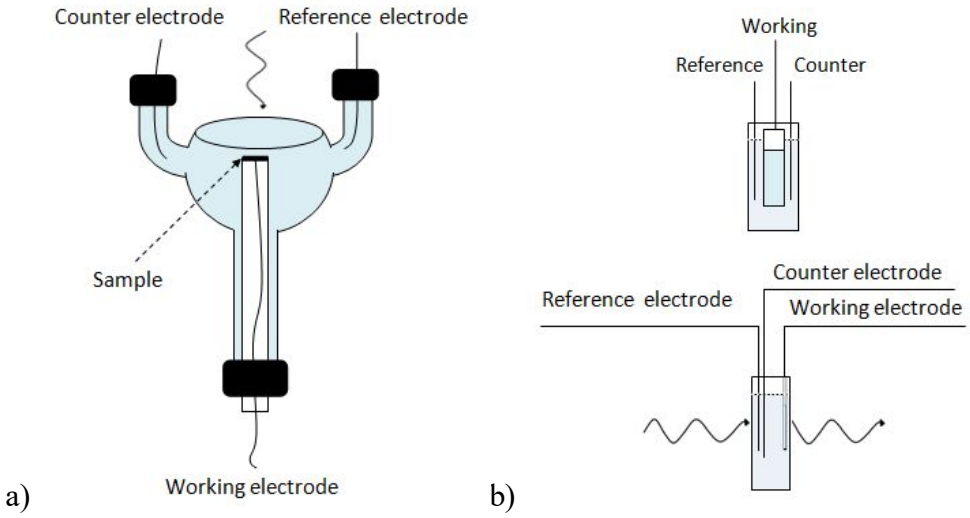

Figure 5. The spectroelectrochemical cell assembling a) for Raman studies, b) for UV-Vis measurements

4. Results and discussion

4.1 Investigation of lithium insertion into TiO_2 polymorphs

4.1.1 Li^+ insertion into anatase {101} vs {001}

The first comparative studies of anatase facets {101} and {001} were carried out on macroscopic single crystals by Hengerer et al.[58] Higher activity for Li^+ insertion was observed for the exposed crystal facet {001}. This work was motivation for our investigation of Li^+ insertion behavior of nanocrystalline anatase {101} and {001} electrodes (**Appendix 1**).[17] The main results of the work in **Appendix 1**[17] are as follows:

SEM image and XRD pattern of synthesized anatase nanocrystals with most exposed facet {001} are shown in Figure 6. The morphology of nanoplatelets typical for anatase with predominant facet {001} is visible from the SEM image. Theoretical surface area of nanosheets based on crystals dimensions (~50 nm x 50 nm x 8 nm) was 85 m^2/g and the measured S_{BET} surface area was 68 m^2/g. Common synthetic protocol for preparation of anatase nanosheets with preferred orientation {001} is based on hydrothermal treatment in hydrofluoric acid as a morphology directing procedure (see Experimental section). Therefore our synthesized anatase

nanosheets were tested for presence of fluorine by EDX. As prepared material exhibited 8 wt % of F, but concentration of F was negligible after calcination of the powder at 450 °C for 30 min.

Li^+ insertion behavior of anatase {001} nanocrystals was compared with behavior of two anatase {101} materials C240 and P90 with surface areas close to our nanosheets (see Experimental section). Cyclic voltammograms (CVs) at scan rates from 100 mV/s to 0.1 mV/s were measured in a range of potentials from 1.3 V to 2.5 V against Li/Li^+ reference electrode. The comparison of cyclic voltammograms of the prepared anatase nanosheets {001} and anatase C240 is shown in Figure 7 for scan rate 0.2 mV/s. The voltammograms confirmed phase purity of both anatase materials by a presence of just one pair of peaks. The anatase {001} exhibited lower peak-to-peak splitting compared to anatase C240. Indirect proportionality between peak-to-peak splitting and nanocrystals' surface area was observed in the past for anatase materials. But in our case the anatase {001} had this splitting lower in spite of its smaller surface area compared to C240. Therefore these data indicated improved Li^+ insertion in the anatase {001} material.

We calculated charge capacities, *C*, of the measured materials from voltammetric data. The capacities were 616 C/g for anatase {001}, 550 C/g for C240 and 570 C/g for P90. Overall charge stored in anatase {001} electrode was obviously higher than amount of Li^+ inserted into the same mass of C240 or P90 material.

Furthermore, kinetic analysis of cyclic voltammograms revealed fundamental differences in diffusion coefficients of Li, $D_{Li,}$ for anatase {001} compared to C240 and P90. The analysis is based on relation between voltammetric peak current *Ip* and scan rate *v* for diffusion-controlled charge transfer:

$$(Ip) = 0.4958nFAc(D_{Li}\alpha nFv/RT)^{1/2} \quad (4)$$

where *n* is the number of electrons, *A* is the electrode area, *c* is the maximum concentration of lithium ions in the accumulation layer (0.024 mol/cm^3 for $x = 0.5$), α is the charge-transfer coefficient, and the other symbols have their usual meaning. The fitting of *I*p dependencies on $v^{1/2}$ enabled us determination of diffusion coefficient of Li^+ for studied materials. The calculated

D_{Li} for anatase nanosheets was 1.33×10^{-18} cm^2/s, which was approximately of one order higher than coefficients determined for C240 ($D_{Li} = 4.89 \times 10^{-19}$ cm^2/s) and P90 ($D_{Li} = 4.65 \times 10^{-19}$ cm^2/s).

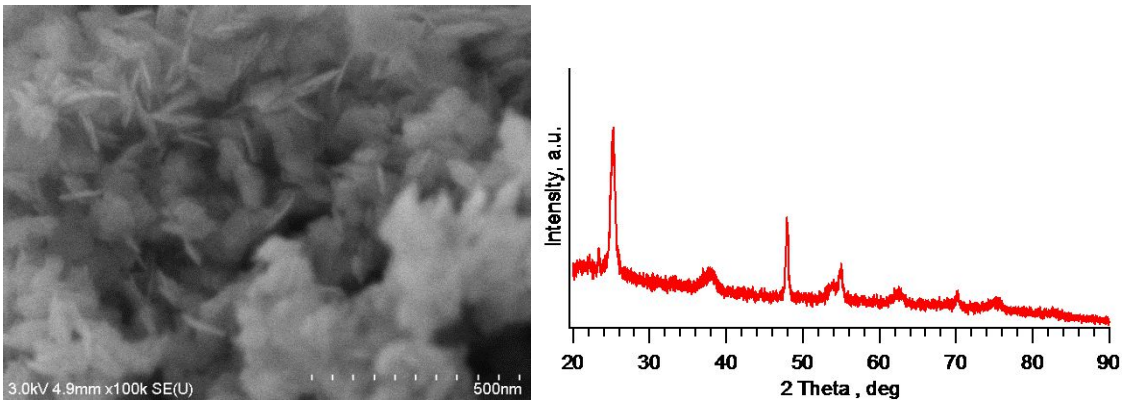

Figure 6. SEM image (on the left) and X-ray diffractogram (on the right) of synthesized anatase {001} nanosheets.

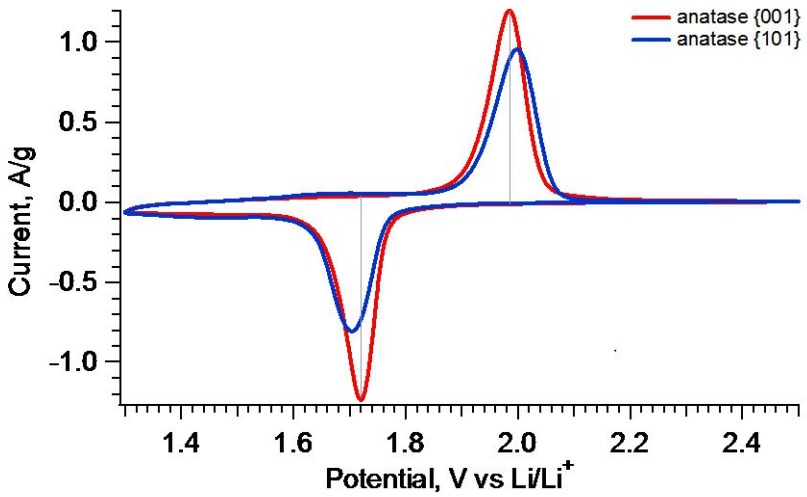

Figure 7. The cyclic voltammograms of nanocrystalline anatase exposing mainly the {001} facet (red line) and anatase C240 with predominant the facet {101} (blue line) in 1 M $LiN(CF_3SO_2)_2$ + EC/DMC (1/1 by mass) at scan rate 0.2 mV/s. The gray lines signify the position of insertion/extraction peak maxima of anatase {001} just to show lower peak-to-peak splitting compared to C240.

Subsequently, chronoamperometry (CHA) was carried out on anatase films. The potentials from 1.3 V to 3 V and back were applied on electrodes with waiting time of 1000 s at

each potential step. D_{Li} can be calculated from currents from Li^+ insertion and extraction branch of chronoamperometric curve according to Cottrell equation, which is partially valid also for polycrystalline electrodes (For more information please see **Appendix 1**[17]). The calculated CHA diffusion coefficient of Li^+ for anatase nanosheets was 5.43×10^{-15} cm^2/s, which was again higher than calculated coefficients for C240 ($D_{Li} = 3.20 \times 10^{-15}$ cm^2/s) and P90 ($D_{Li} = 3.40 \times 10^{-15}$ cm^2/s). The diffusion coefficients determined by CHA have larger values by orders of magnitude in comparison with the values from cyclic voltammetry data. This can be accounted to different electrical field after the potential step and to different time and process of data collection for both methods.[59, 60]

Further, chronoamperometry was measured for various temperatures and thus the diffusion coefficients of Li^+ for different temperatures were determined. Because temperature dependence of D_{Li} is of Arhenius-type ($D = D_0 \exp(-E_a/kT)$), these measurements enabled us calculation of activation energy (E_a) for lithium insertion for all studied materials. The activation energy of nanocrystaline anatase {001} was determined as 0.09 eV and it was lower than found activation energies of C240 (0.17 eV) and P90 (0.14 eV).

All these data indicate more facile insertion of lithium into anatase nanoplatelets with predominant facet {001} compared to ordinary anatase nanocrystals. These results for nanocrystalline electrodes are in a good agreement with the anisotropy of Li^+ insertion previously observed on macroscopic single crystal electrodes with exposed facets {101} and {001}.[58] The explanation of the observed higher activity of facet {001} to Li^+ insertion is facile Li^+ diffusion in the direction parallel to *c*-axis, which is a consequence of different number of the Li^+ hopping events between pseudooctahedral positions in the anatase lattice.[17, 58]

4.1.2 Li^+ insertion into anatase {101} vs TiO_2 (B)

Standard anatase {101} nanocrystalline electrodes served as reference electrodes in our next study, where Li^+ insertion properties of new promising material TiO_2 (B) were investigated. This part of thesis follows the work of Zukalova et al.,[9] where peak currents proportional to scan rate were observed during cyclic voltammetry of TiO_2 (B). Such behavior is different than that of anatase materials. Driving force of lithium insertion into anatase is mainly a diffusion and thus peak current proportional to square root of a scan rate is observed in CVs. Faradaic

pseudocapacitance revealed in TiO_2 (B) by Zukalova et al.[9] was attributed to possible accommodation of Li^+ in TiO_2 (B) open channels along the *b*-axis, which enables facile transport of lithium in TiO_2 (B) structure. Generally, overall charge connected with Li^+ storage in TiO_2 is superposition of two contributions. The first one is a lithium insertion into the bulk, which is controlled by diffusion and dominates in anatase. The second one is a capacitive charging of double-layer, which plays role mainly for materials with a large surface area as in the case of anatase nanocrystals. The pseudocapacitive charge storage in the bulk of TiO_2 (B) observed by Zukalova et al.[9] is inconsistent with some works, where a square-root dependence of voltammetric peak current on scan rate or both possibilities ($Ip \approx v$ and $Ip \approx v^{1/2}$) were reported for TiO_2 (B).[61, 62] This contradiction motivated our detailed study of differences in charging mechanisms of anatase and TiO_2 (B) during Li^+ insertion (**Appendix 2**).[26] The main results of the work in **Appendix 2**[26] are as follows:

Four materials were tested in this study, the TiO_2 (B) coded as TBa, anatase C240, P90 and an approximately half-and-half mixture of TiO_2 (B) and anatase coded as N21 (see Experimental section). The phase purity of our synthesized TiO_2 (B) material was confirmed by XRD pattern, which corresponded to standard TiO_2 (B) diffractogram (JCPD No. 35-0088) without anatase features (**Appendix 2**[26]). The Raman spectrum consisted of vibrational bands characteristic for TiO_2 (B) with no recognizable anatase peaks (**Appendix 2**[26]). The SEM image of TBa with a fibrous structure typical for TiO_2 (B) is shown in Figure 8a.

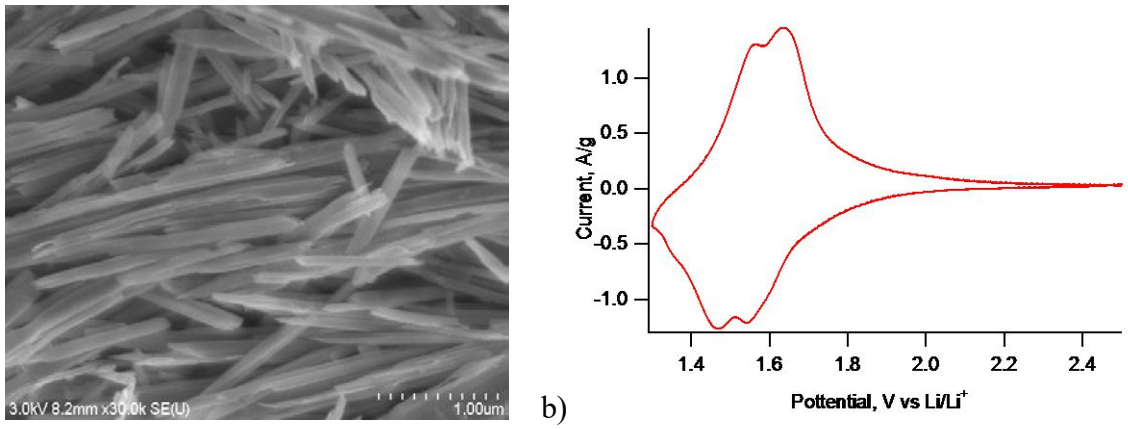

Figure 8. The synthesized TBa material: a) the SEM image and b) the cyclic voltammogram at scan rate 0.5 mV/s in 1M $LiN(CF_3SO_2)_2$ + EC/DME (1/1 by mass).

Electrodes with the same mass of active material were prepared from these powders and cyclic voltammetry was applied in a common range of potentials (1.3 V – 2.5 V against Li/Li^+) at various scan rates. A cyclic voltammogram of TBa at scan rate 0.5 mV/s is shown in Figure 8b. It demonstrates phase purity of TBa material again, because of absence of any anatase features. Subsequently, measured voltammograms were processed by technique of cyclic voltammograms deconvolution previously reported by Dunn et al.[63, 64] for anatase materials. A main idea of this method consists in expression of overall current response at fixed potential $i(V)$ as combination of two separate terms with different scan rate, v, dependency.

$$i(V) = k_1 v + k_2 v^{1/2} \quad (5)$$

The first one corresponds to current connected with fast capacitive processes on the TiO_2 surface and with pseudocapacitive Li^+ storage in the bulk. The second one is a contribution of currents caused by diffusion-controlled insertion processes. The Equation 5 can be transformed to linear dependence $i(V)/v^{1/2} = k_1 v^{1/2} + k_2$ and the coefficients k_1 and k_2 can be easily determined from linear fitting of CV data at each potential.

We chose cyclic voltammograms at scan rates from 4 mV/s to 0.1 mV/s for this evaluation, because of adequate identification of voltammetric peaks of all the samples for this range of scan rates. We determined the coefficients k_1 and k_2. When the coefficients k_1 and k_2 are known, then the ratio of the contribution of capacitive current ,i_c, to the total current can be calculated for each material as $i_c = k_1 v$. The calculated ratios of i_c contributions to the overall voltammetric currents of phase pure samples TBa and C240 are shown in Figure 9 for voltammograms at scan rate of 0.5 mV/s.

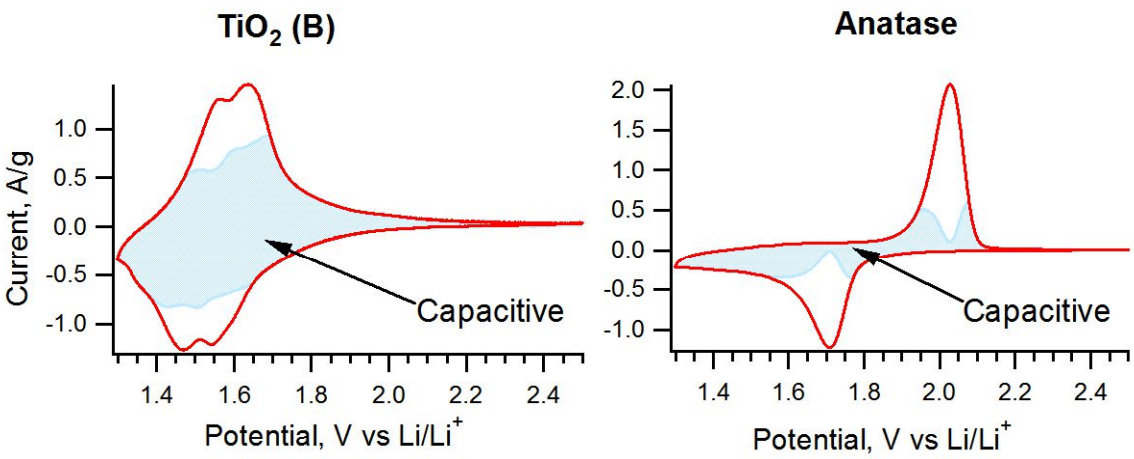

Figure 9. Cyclic voltammograms of TiO_2 (B) (sample TBa) and anatase (sample C240). The voltammograms are displayed for a scan rate of 0.5 mV/s. Red lines correspond to experimentally obtained voltammetric currents. Blue areas represent calculated capacitive contributions.

The ratios of i_c contributions to the total current response of materials at a relatively slow scan rate 0.5 mV/s were determined as: 68% for TBa, 37% for C240, 41% for P90, 38% for anatase part of N21 material and 72% for TiO_2 (B) part of N21. The capacitive contributions of anatase materials are in good agreement to each other as well as contributions of TBa and TiO_2 (B) part of N21. Observed capacitive contributions are of about 30% higher in TiO_2 (B) compared to anatase materials. It demonstrates, that even at slow scan rates the capacitive currents play obviously much significant role for TiO_2 (B) than for anatase.

Such behavior is interesting when one takes into consideration the three times lower surface area of phase pure TiO_2 (B) material compared to anatase samples (see Experimental section). If we associate capacitive contribution with crystal surface processes only, than we can expect a direct proportionality between these two quantities. Dunn et al.[63, 64] confirm this behavior for anatase nanocrystals of different sizes, where higher capacitive contributions for higher surface areas were observed. However, our data obviously contradict this conclusion and indicate that capacitive charge storage in TiO_2 (B) does not occur on surface only. Therefore, these results evidently support the assumption of Zukalova et al.[9] about faradaic pseudocapacitive accommodation of Li^+ in TiO_2 (B) open channels.

Furthermore, the total stored charge at scan rate 0.5 mV/s was 625 C/g in TBa sample, which was of about 27% higher than overall charge stored in anatase C240 (435 C/g) and P90

(465 C/g). This difference in the total stored charge is close to observed differences in capacitive contribution. On the basis of all these data we can suppose, that the accommodation of lithium in TiO_2 (B) open channels is pseudocapacitive process which most likely causes the main difference in electrochemical response of TiO_2 (B) and anatase and is responsible for higher level of inserted lithium in TiO_2 (B) compared to anatase.

Current maxima of extraction peaks were analyzed separately and capacitive/diffusion contributions were determined for each scan rate for all the samples. The change of capacitive and diffusion contributions to overall current with scan rates was investigated. In the case of TiO_2 (B), the capacitive contribution higher than diffusion one was observed for a large range of scan rates until 0.5 mV/s. On the other hand, for anatase materials, the diffusion-controlled currents were dominant for all measured scan rates (**Appendix 2**[26]). The high capacitive contributions to the total currents in extraction peak maxima of TBa even at slow scan rates indicates high level of pseudocapacitive Li^+ storage in TiO_2 (B) too.[26, 65]

4.1.3 In situ Raman spectroelectrochemistry of isotope-labeled materials

Improved lithium insertion properties of anatase {001} compared to anatase {101} discussed in the section 4.1.1 show that shape of crystals has an influence on Li^+ insertion rates. This fact represented a challenge for us to carry out deeper analysis of structural changes in anatase during lithium insertion (**Appendix 3**[32]). We choose Raman and in-situ Raman spectroelectrochemistry as suitable methods for this study. The latter is a technique based on recording of Raman spectra of a material during electrochemical measurement, for example electrochemical lithium insertion. The phase transition from tetragonal anatase to orthorhombic lithium titanate Li_xTiO_2 ($x \approx 0.5$) occurs during Li^+ insertion (see section 1.1.1). TiO_2 anatase has six Raman active vibrations, $A_{1g} + 2B_{1g} + 3E_g$. Raman spectra of lithium titanate were reported earlier,[66-68] however, some discrepancies concerning actual number and positions of new Raman lines appearing after Li^+ insertion into anatase still remained. Thus, the unequivocal assignment of the particular bands was unknown. Solution of this problem can be found by use of isotope labeled compounds during measurements, because different mass of particular isotopes can lead to shifts of some vibrational bands. Hence, labeling is useful method for determination of vibrational modes involving any contribution of the element used as isotopic label.

Raman spectrum of a phase pure TiO_2 anatase containing different oxygen isotopes (^{16}O, ^{17}O, ^{18}O), has been already measured and calculated.[69, 70] An isotope shift of all anatase vibrations (A_{1g}, $2B_{1g,}$ and $3E_g$) for oxygen isotope labeled samples (^{17}O, ^{18}O) was determined experimentally and numerically. The maximal theoretical isotopic shift of vibrational bands of ^{18}O-labeled samples is 5.7% referenced to those of the ^{16}O-labeled samples.[69] This value predicts what would be the maximal shift for each vibrational mode, if this mode had contribution only from oxygen motions. Contributions of titanium motion 0 and 0.0088 were calculated for anatase vibrational modes A_{1g} and $E_g(3)$ respectively. Hence, these two vibrations of anatase $Ti^{18}O_2$ should have isotopic shifts close to maximal theoretical shift for oxygen ^{18}O.

The main results of the work in **Appendix 3**[32] are as follows:

Oxygen ^{18}O isotope labeled anatase $Ti^{18}O_2$ and standard one $Ti^{16}O_2$ were synthesized and particular electrodes were prepared (see Experimental section). Phase purity of samples was confirmed by their XRD patterns and morphology tested by SEM images. The electrodes were placed in spectroelectrochemical cells and potentials from -0.2 V to -1.6 V vs Ag/AgCl were applied. The Raman spectra were acquired in a potentiostatic regime with equilibration time of 3 min at each potential step. In this part of study lithium perchlorate $^7LiClO_4$ was used as an electrolyte (see Experimental section). The spectra of $Ti^{18}O_2$ and $Ti^{16}O_2$ electrodes were measured at potential -0.2 V, where no lithium insertion occurred. The peak shifts of oxygen isotope labeled anatase for particular vibrational modes are presented in Table 1. The shifts of vibrational bands A_{1g} and $E_g(3)$ show, that our isotope labeled material was pure $Ti^{18}O_2$ anatase (*vide supra*).

Mode	$E_g(1)$	$E_g(2)$	$B_{1g}(1)$	$B_{1g}(2)$, A_{1g}	$E_g(3)$
position for $Ti^{16}O_2$ [cm^{-1}]	145	197	397	517	639
ν_{16}-ν_{18} [cm^{-1}]	1	10	1	29	36.5
ν_{16}-ν_{18} [cm^{-1}] calc.[69, 70]	1	8	0	28.8, 30.1	37

Table 1. Differences in positions of Raman bands in anatase $Ti^{16}O_2$ and $Ti^{18}O_2$ obtained experimentally and previously calculated shifts for comparison.

The evolution of Raman spectra during spectroelectrochemistry of $Ti^{18}O_2$ is presented in Figure 10. Raman bands of orthorhombic lithium titanate Li_xTiO_2 were distinguishable at

potentials around -1 V (insertion coefficient x ≈ 0.05) and increased in intensity for more negative potentials during Li^+ insertion, but slowly diminished for potential -1.3 V (x ≈ 0.3) and lower. In spite of disappearance of features of orthorhombic phase in Raman spectra at -1.6 V (x ≈ 0.4), original spectrum of this phase and subsequently tetragonal anatase phase was restored again in extraction regime. This proves a good reversibility of our electrodes. The Raman spectrum of $Li_xTi^{16}O_2$ is shown in Figure 11a. The spectrum was deconvoluted using Lorentzian peak shapes.

Raman spectra of lithium titanates ($Li_xTi^{16}O_2$ and $Li_xTi^{18}O_2$) acquired at -1.25 V were compared (Fig.11b). On the basis of isotopic shifts we can conclude that all peaks in orthorhombic lithium titanate spectrum have certain contribution of oxygen atom movement, but this is different for each vibration. Isotopic shifts close to the theoretical maximum 5.7% were observed for six peaks p9, p12, p13, p15, p16 and p17 (Figs.11a, 11b), which indicate the vibrations caused predominantly by oxygen motions. In addition, analogous measurements of $Ti^{18}O_2$ and $Ti^{16}O_2$ electrodes in isotope labeled electrolyte solution followed. The $^6LiClO_4$ served as source of ^6Li in electrolyte solution. Raman spectra of lithium titanates ($^7Li_xTi^{16}O_2$ and $^6Li_xTi^{16}O_2$) acquired at potential -1.25 V are shown in Figure 11c. Isotopic shifts of peaks between $^7Li_xTi^{16}O_2$ and $^6Li_xTi^{16}O_2$ (alternatively $^7Li_xTi^{18}O_2$ and $^6Li_xTi^{18}O_2$) were analyzed. Maximal theoretical isotopic shift for ^6Li vs ^7Li of 7.4 % was calculated. Zero shifts were observed for peaks p1, p2, p8, p9, p10 and p17. Shifts of all other vibrations were much lower than theoretical maximum. This can be explained by Coulombic repulsion of lithium ions in the lattice, which leads to hindering of Li^+-Li^+ interaction.

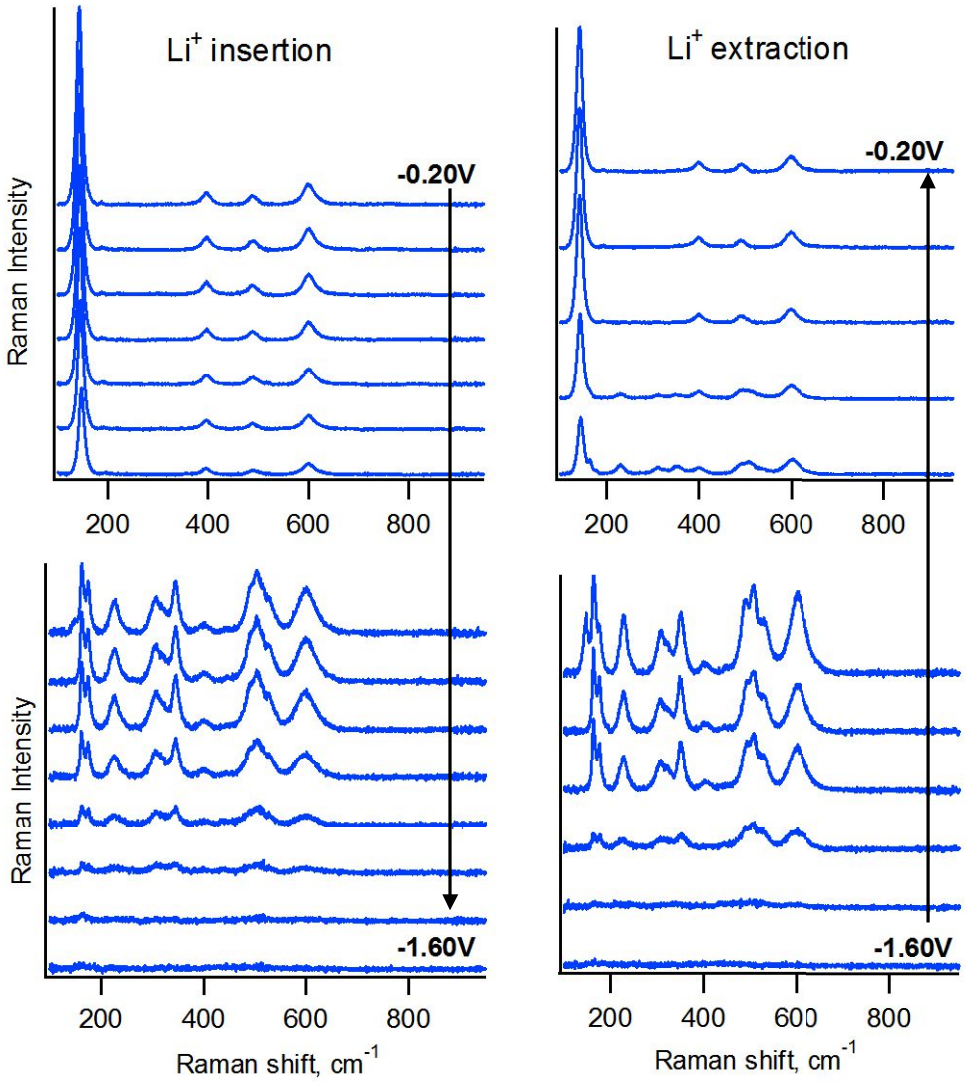

Figure 10. In situ Raman spectra of $Ti^{18}O_2$ during $^7Li^+$ insertion (on the left - decreased potentials for the curves from top to bottom), and extraction (on the right- bottom to top) in 1 M $^7LiClO_4$ + EC/DMC (1/1). Potential values are against Ag/AgCl. Potential intervals beween presented spectra were not equidistant (for details see **Appendix 3**[32])

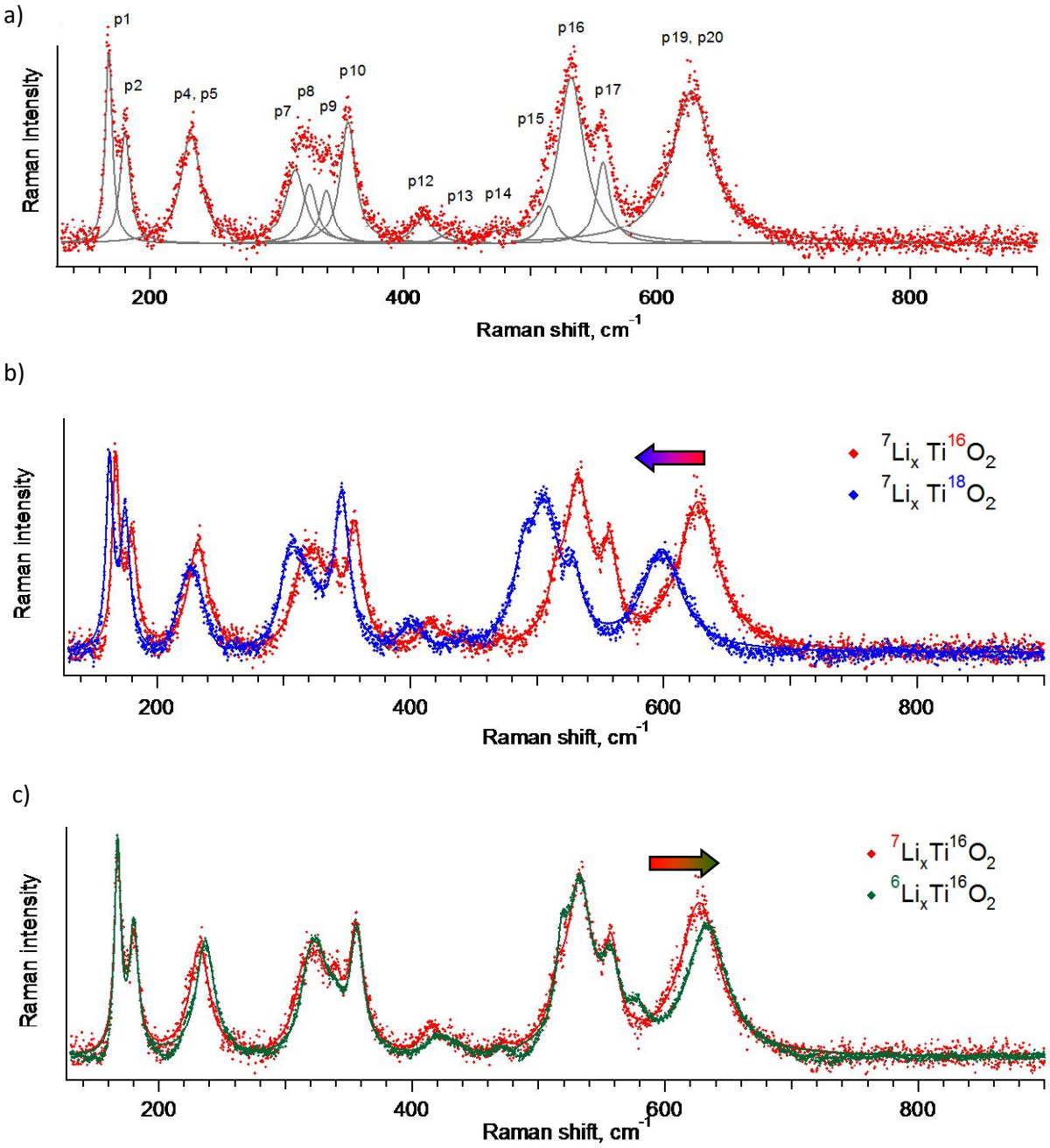

Figure 11. a) In situ Raman spectrum of $Li_xTi^{16}O_2$ measured at -1.25 V vs. Ag/AgCl (red points) with individual Lorentzian components (solid lines). b) In situ Raman spectra of $Li_xTi^{16/18}O_2$ evolved by lithium insertion into anatase $Ti^{16}O_2$ (red points) and anatase $Ti^{18}O_2$ (blue points) at -1.25 V vs. Ag/AgCl. c) In situ Raman spectra of $^{6/7}Li_xTi^{16}O_2$ evolved by lithium $^{7}Li^{+}$ (red points) or $^{6}Li^{+}$ (green points) insertion into anatase $Ti^{16}O_2$ at -1.25 V vs. Ag/AgCl. Arrows indicate the direction of shifts caused by isotope substitution.

In situ spectroelectrochemical measurements were supplemented by ex situ measurements at room temperature and at 77 K. For this purpose chemically lithiated samples

were prepared using *n*-butyllithium with a natural abundance of Li isotopes. $Ti^{16}O_2$ and $Ti^{18}O_2$ were stirred in a 1.6 M solution of *n*-butyllithium in hexane with a Li/Ti molar ratio of 2.5 resulting in $^{7}Li_xTi^{16}O_2$ and $^{7}Li_xTi^{18}O_2$ powders. The $^{6}Li_xTi^{16}O_2$ and $^{6}Li_xTi^{18}O_2$ samples for ex situ measurements were prepared by electrochemical $^{6}Li^{+}$ insertion into $Ti^{16}O_2$ or $Ti^{18}O_2$. Ex-situ spectra of studied samples were measured in a hermetically closed optical cell to avoid any contact with air. Cooling by liquid nitrogen was used for low temperature measurements. Spectra of the orthorhombic lithium titanate acquired ex situ were characterized with higher resolution than in situ spectra. It helps to distinguish some peaks as p4, p5 and p19, p20. However, the best spectral resolution was achieved for low-temperature spectra. The examples of ex situ Raman spectra of $^{6/7}Li_xTi^{16}O_2$ measured at 77 K are shown in Figure 12. Some low-temperature spectra exhibited contamination by TiO_2 (anatase). The reason for this can be air-oxidation during manipulation with samples, caused by sensitivity of lithium titanate to air. Therefore the in situ Raman spectroelectrochemistry is more favorable for room temperature measurements.

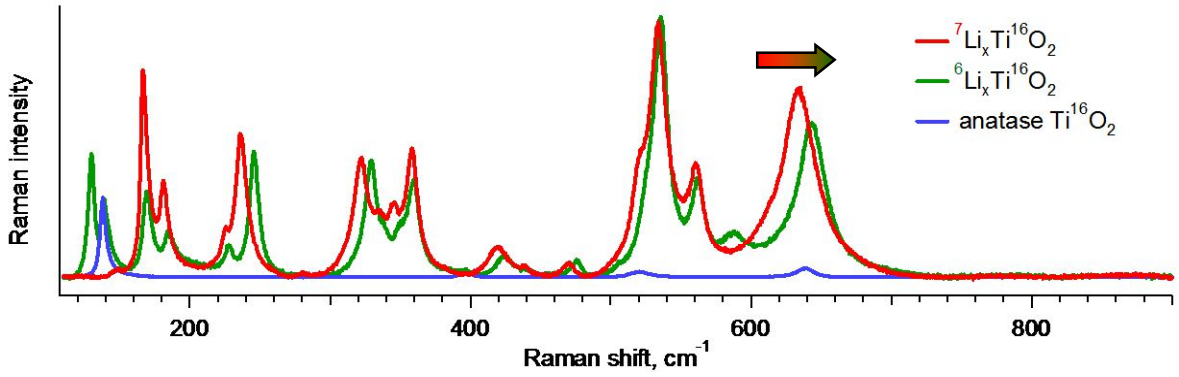

Figure 12. Ex-situ Raman spectra of lithium titanate prepared from $Ti^{16}O_2$ by electrochemical lithiation (^{6}Li, green line) or chemical lithiation with n-butyllithium (^{7}Li, red line). Anatase $Ti^{16}O_2$ impurity is also seen in $^{6}Li_xTi^{16}O_2$. The spectrum of anatase $Ti^{16}O_2$ (blue line) is added for comparison. Spectra of $^{6/7}Li_xTi^{16}O_2$ were measured at 77 K. The peak at ca. 125 cm^{-1} (green line) is unassigned. Since it does not appear in the same in situ Raman spectra, we ascribe it to unknown impurity in this particular sample, $^{6}Li_xTi^{16}O_2$. Arrow indicates the direction of shifts caused by isotope substitution.

Above mentioned measurements supported by theoretical DFT calculations enabled the deconvolution of lithium titanate spectra. As a result, we found 20 peaks in the Li_xTiO_2 spectrum. This number is higher than number of modes predicted by Hardwick et al.[68], but it is lower than 42 vibrations ($14A_g + 14B_{1g} + 7B_{2g} + 7B_{3g}$) expected by our DFT calculations. Lower number of observed bands can be due to their low intensity which makes them undetectable

under our experimental conditions. DFT calculations could not provide information about intensities of peaks owing to metallic character of material, but calculated positions of bands and their isotopic shifts enabled us an assignment of observed Raman bands to particular vibrational modes. The assignment of $^{7}Li_xTi^{16}O_2$ peaks to symmetries of the calculated vibrations is summarized in Table 2.

peak	p1	p2	p3	p4	p5	p6	p7	p8	p9	p10
ν [cm^{-1}]	167.3	181.2	200.7	224.8	236.6	280.4	321.8	334.8	345.3	358.4
sym.	B_{3g}	A_g	B_{1g}	A_g	B_{1g}	B_{2g}	B_{1g}	A_g	A_g	B_{1g}
peak	p11	p12	p13	p14	p15	p16	p17	p18	p19	p20
ν [cm^{-1}]	382	419.7	437.8	469.9	519.9	533.8	560.4	569.4	610	634.4
sym.	B_{3g}	B_{1g}	B_{1g}	A_g	A_g	A_g	B_{2g}	B_{1g}	A_g	B_{1g}

Table 2. Positions of $^{7}Li_xTi^{16}O_2$ peaks in Raman spectrum, which was acquired at 77 K. The peaks are assigned to symmetries of the DFT calculated vibrations.

4.1.4 In situ Raman spectroelectrochemistry of TiO_2 (B) and rutile

We found that above described technique of in situ Raman spectroelectrochemitry is an useful tool for detection of anatase impurities in TiO_2 materials (**Appendix 4**[29]). Three the most applicable TiO_2 polymorphs are anatase, rutile and TiO_2 (B) (see Section 1.1). Phase purity of samples is important especially in the case of evaluation of physicochemical properties of TiO_2 materials. Contamination of rutile and TiO_2 (B) powders by anatase phase from synthesis is not unusual.[11, 71, 72] XRD and Raman spectroscopy are common methods for determination of phase purity of materials. However, these techniques have certain limits in the case of TiO_2 materials. XRD sensitivity to low anatase impurities is reduced for thin layers and anatase crystal size in nanometer units. Moreover, the most intensive diffraction peak of anatase 25° (2 Theta) is in overlap with a TiO_2 (B) peak. A similar problem is observed for Raman spectra of TiO_2 (B) and rutile. Rutile has four first-order Raman modes $A_{1g} + B_{1g} + B_{2g} + E_g$ and TiO_2 (B) has 18 Raman-active vibrations: $12A_g + 6B_g$. Both modifications have vibrational bands ($A_g(2)$ of TiO_2 (B) and B_{1g} of rutile) at 144 cm^{-1}, which is a position of the most intensive Raman peak $E_g(1)$ of anatase. This overlap significantly complicates the detection of possible anatase impurities in both polymorphs. Therefore, we studied two TiO_2 (B) materials and one rutile sample by in situ Raman spectroelectrochemisty of lithium insertion (**Appendix 4**[29]).

The details of this part of thesis are in **Appendix 4**[29]. Briefly: The Raman spectra were acquired during cyclic voltammetry at scan rate 0.5 mV/s for rutile electrode and 0.2 mV/s for TiO_2 (B) electrodes. No voltammetric peaks assignable to Li^+ insertion into anatase were observed in the voltammograms of the samples. Evolution of Raman spectra during Li^+ insertion into the first TiO_2 (B) material TBa can be described as a gradual diminishing of TiO_2 (B) Raman features without observation of new ones. Subsequent Li^+ extraction leads to a recovery of TiO_2 (B) Raman spectrum. The situation for a second TiO_2 (B) material TBb was different and typical Raman spectrum of orthorhombic lithium titanate Li_xTiO_2 showed up in a process of Li^+ insertion into the material. Analogous result as that for TBb sample was observed for the rutile electrode. An acquired XRD pattern, cyclic voltammogram at 0.5 mV/s and an example of in situ Raman spectrum for the rutile sample are demonstrated in Figure 13.

The presence of Raman features of orthorhombic lithium titanate in spectroelectrochemical data of rutile and TBb samples we attributed to small anatase impurities in these materials, which are hardly detectable by XRD and common Raman spectroscopy due to the reasons discussed above. Moreover, such phase sensitive method as cyclic voltammetry was not able to distinguish these impurities too (Fig. 13b). Hence our study shows excellent sensitivity of Raman spectroscopy to low concentrations of orthorhombic lithium titanate in measured samples and it is possible to conclude that in situ Raman spectroelectrochemistry enables a detection of small anatase impurities in TiO_2 materials through evolution of Li_xTiO_2 Raman features during Li^+ insertion.

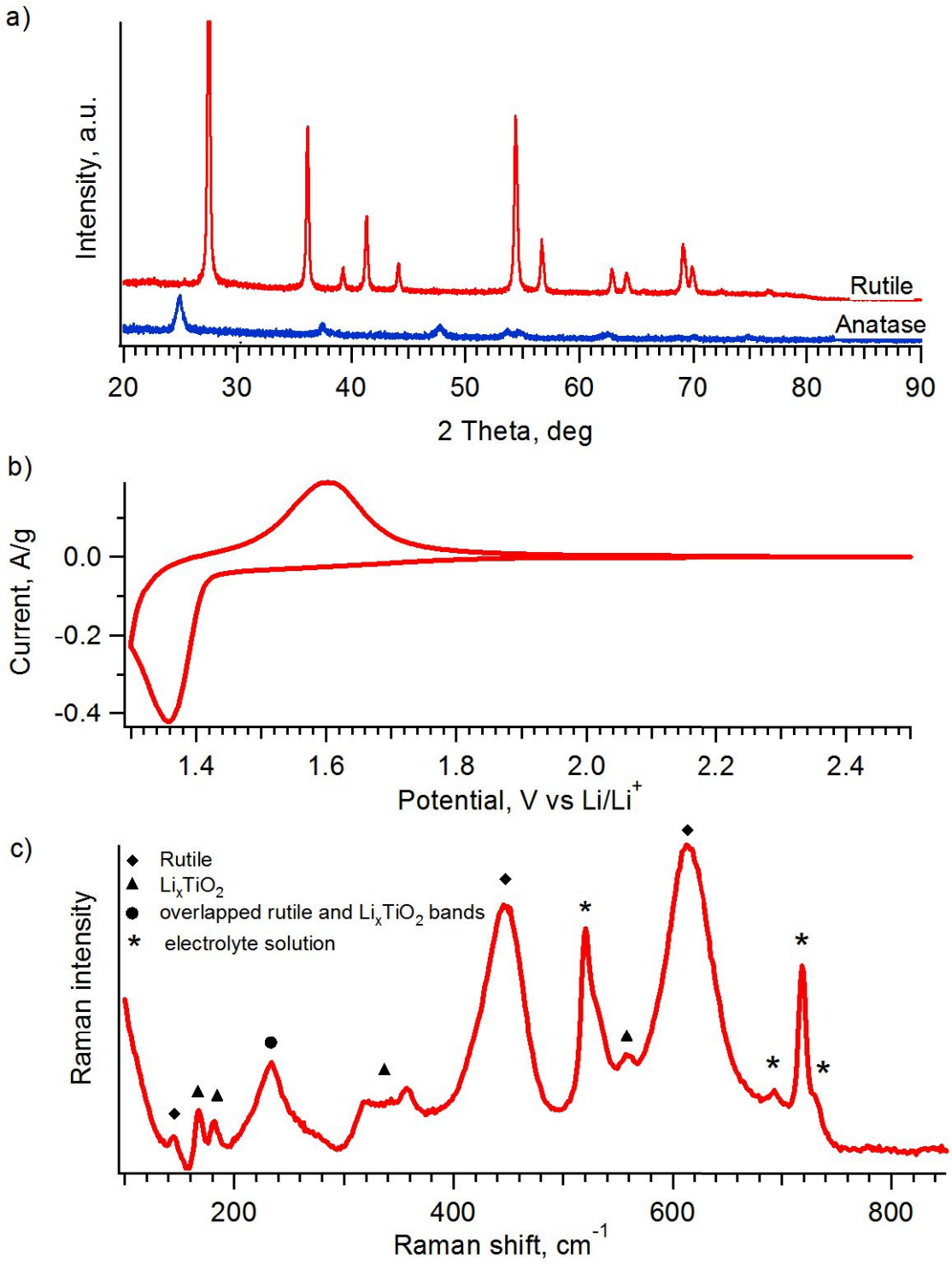

Figure 13. a) XRD difractogram of rutile sample compared to XRD pattern of anatase C240. b) Cyclic voltammogram of lithium insertion into the rutile in 1 M $LiN(CF_3SO_2)_2$ + EC/DMC (1/1 by mass). c) In situ Raman spectrum of the rutile electrode in 1 M $LiClO_4$ + EC/DMC (1/1) during cyclic voltammetry at potential 1.87 V against Li/Li^+.

4.2 Sodium insertion into $Li_4Ti_5O_{12}$

High sensitivity of Raman spectroscopy to orthorhombic lithium titanate Li_xTiO_2 (arisen during Li^+ insertion into anatase) is not constrained only to detection of anatase impurities in rutile and TiO_2 (B) discussed in previous section. In our recent work, studying of sodium insertion into $Li_4Ti_5O_{12}$ spinel, detailed Raman spectroscopy analysis was used to confirm a presence of anatase impurities in $Li_4Ti_5O_{12}$ (**Appendix 5**[46]). Spinel lithium titanate $Li_4Ti_5O_{12}$ is another attractive material for applications in batteries due to its structure and relatively high potential preventing formation of dendrites (see section 1.2). Na^+ storage is studied during last few years as a novel promising system for energy accumulation in batteries. In our study Na-insertion properties of a synthesized nanocrystalline $Li_4Ti_5O_{12}$ spinel (nanoLTS) were compared with the behavior of commercial spinel lithium titanate (**Appendix 5**[46]).

Briefly, sodium insertion into $Li_4Ti_5O_{12}$ electrodes was investigated by cyclic voltammetry. Changes in the cyclic voltammograms of nanoLTS were observed during long lasting cycling. An analysis of nanoLTS electrode after Na-insertion was carried out by Raman spectroscopy. The presence of orthorhombic lithium titanate features typical for Li^+ insertion into anatase in Raman spectrum of nanoLTS after Na^+ insertion was revealed. Subsequently, the minor anatase impurities in nanoLTS were detected after detailed analysis. The proved presence of anatase impurities in the sample led to probable explanation of observed changes in nanoLTS cyclic voltammograms. Because no vibrational bands analogous to $Li_{0.5}TiO_2$ were observed during testing of phase pure anatase electrode after Na-insertion, we can suppose that the presence of orthorhombic phase in nanoLTS after cycling is a consequence of release of the Li^+ from parent material ($Li_4Ti_5O_{12}$) and its subsequent accommodation in anatase structure. The Na^+ insertion into nanoLTS is obviously accompanied by partial Li redistribution into minor anatase impurities and this process results in observed changes of nanoLTS ability to accommodate Na^+.

4.3 Flatband potential and electron kinetics of TiO_2 anatase {101} vs {001}

In section 4.1.1 the anatase {001} nanosheets were demonstrated to have a better performance during Li^+ insertion than anatase {101} nanoparticles. In addition they have better

properties than anatase {101} nanoparticles in other applications too (photocatalysis). Due to this fact we investigated differences in flatband positions and electron energetics of both anatase nanocrystals orientations together with their properties as photoanodes in DSSCs (**Appendix 6**[18] and **Appendix 7**[19]). The main results of the works in **Appendix 6**[18] and **Appendix 7**[19] are as follows:

On the beginning, the ethanolic and aqueous films were prepared from nanocrystalline anatase {101} and {001} and were tested as photoanodes for DSSCs (see Experimental section and **Appendix 6**[18]). During these tests lower current density and higher open-circuit voltage (V_{OC}) were observed for DSSCs employing anatase {001} as photoanode compared to that with anatase {101} one. Lower current density can be explained by lower amount of dye loaded on the anatase {001} crystals surface. However, clarification of higher V_{OC} needed further investigation. Since the earlier report of accurate impedance data for single crystal electrodes showed negative shift of flatband potential for {001} facet compared to {101} facet (in electrochemical scale),[58] a reason for the V_{OC} enhancement could be different band energetics of nanocrystalline anatase {101} and {001} materials. Therefore we studied possible shift of E_{fb} for our films.

In contrary to single crystals measurements, the Mott-Schottky plots are not suitable for nanocrystalline materials. Hence we adopted a previously developed method of UV-Vis spectroelectrochemistry.[54-56] The technique is based on collection of absorption spectra during electrochemistry. Experimental set up is described in Section 3.4. Principle of our measurements was gradual change of the potential on electrode to more negative potentials and observation of changes of optical absorption spectra with potential. An example of UV-Vis spectra evolution for anatase {001} film is presented in Figure 14 (after subtraction of the spectrum at 0 V). From Fig. 14 it is visible, that differences in optical absorption are not significant until specific potential is reached. This potential corresponds to the flatband potential E_{fb} (see Section 1.1). For more negative potentials than E_{fb} the enhancement of absorption in visible region occurs and so called Burstein shift arises.[54-56] These changes in UV-Vis spectra are caused by setting of accumulation regime in TiO_2 electrode after E_{fb} crossing (see Section 1.1). Therefore an evaluation of increasing absorption of visible light for more negative potentials leads to estimation of E_{fb} position of material. Eventually, our UV-Vis spectroelectrochemical data revealed a negative

shift of the flatband potential for nanocrystalline anatase {001} compared to {101} one (details in **Appendix 6**[18]). This result has been supported later by XPS and UPS data (see **Appendix 7**[19]), which indicated the same bandgap for both orientations and the conduction band upshift by 0.1 eV for anatase {001} powder. (It corresponds to shift to negative potentials in electrochemical scale)

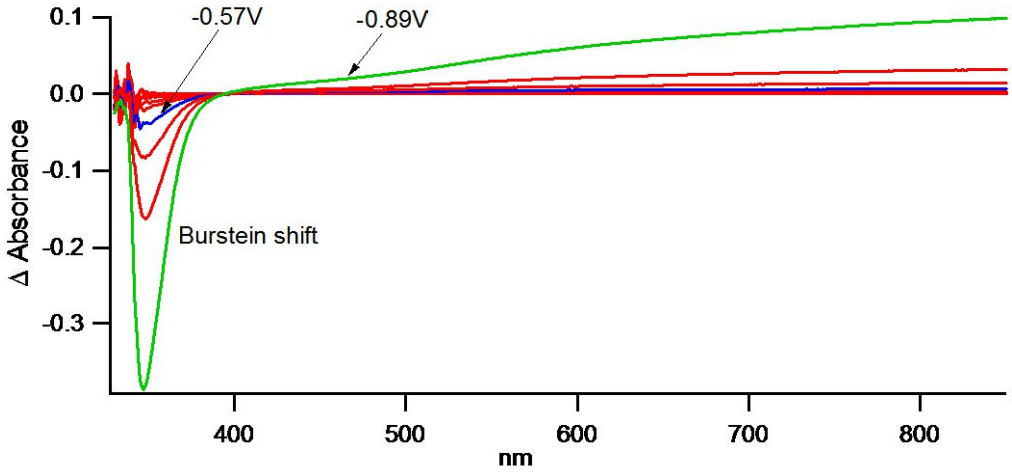

Figure 14. Changes in optical absorption of nanocrystalline anatase {001} electrode during spectroelectrochemistry at pH=3. Differences in absorption for different applied potentials (in V vs. SCE) are presented.

Thereafter we focused on deeper analysis of electron energetics of anatase {101} and {001} **(Appendix 7**[19]**)**. DSSCs with anatase {101} or anatase {001} photoanodes were assembled, as described in Section 3.3, when iodine-based and cobalt-based electrolyte solutions were used for each type of photoanode. Subsequently DSSCs were studied by electrochemical impedance spectroscopy (EIS). EIS measurements were carried out in dark and under illumination. EIS spectra were fitted by transmission line model, what enabled us extraction of three basic parameters from spectra: i) the charge-transfer resistance, R_{ct}, representing the recombination of electrons from TiO_2 by redox couple in electrolyte solution, ii) the chemical capacitance, C_μ, which represents filling of trap states in mesoporous metal oxide and iii) the transport resistance, R_t, of electrons inside TiO_2 material. In addition, if the thickness of active material of photoanode and the porosity of TiO_2 are known and well adjusted, than it is possible to calculate electron lifetime in TiO_2, e^- diffusion coefficient in TiO_2 (D_e), density of states (DOS) etc.

The dependence of R_{ct}, R_t and C_μ on applied potential under illumination for our DSSCs with anatase {101} or anatase {001} photoanodes employing iodine-based electrolyte solution is presented in Figure 15. Our EIS measurements revealed a larger chemical capacitance for anatase {001} nanosheets compared to anatase {101} nanoparticles, which indicates higher amount of electron traps for anatase {001} than for anatase {101}. We confirmed this result by XPS, UPS data and by UV-Vis spectra especially by analysis of Urbach tails of absorption edges (more details in **Appendix 7**[19]**)**.

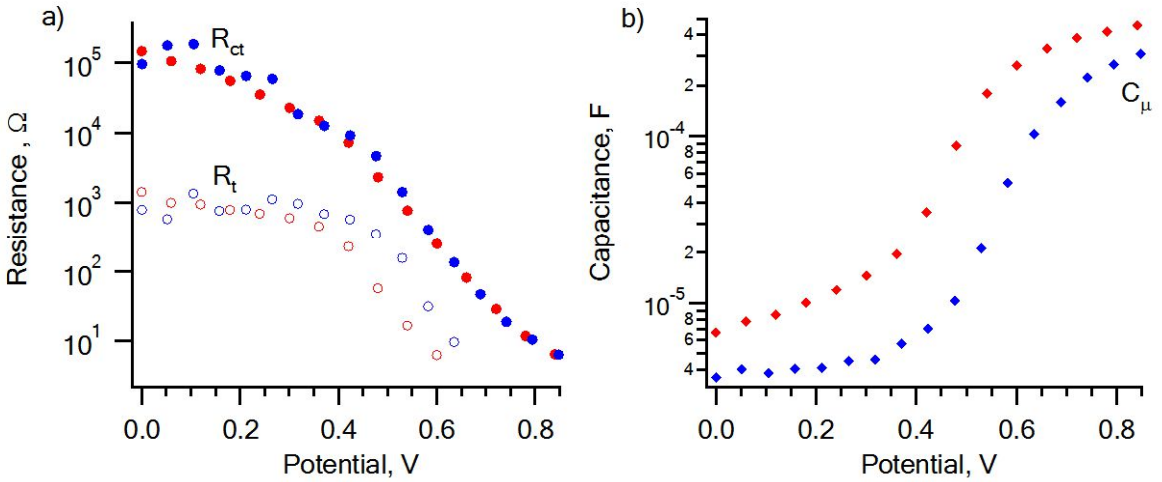

Figure 15. Results from the fitting of electrochemical impedance spectra of DSSCs with iodine-based electrolyte solution under illumination. The devices with anatase {001} photoanode are depicted by red symbols and the devices with anatase{101} photoanode are depicted by blue symbols. a) The potential dependence of charge transfer (R_{ct}, full points) and transport (R_t, circles) resistances in DSSCs. b) The potential dependence of chemical capacitance, C_μ, in DSSCs.

We found, that larger number of electron traps results in higher electron lifetime, τ_e, in anatase {001} material compared to anatase {101}. In this point it is worth mentioning that difference in Voc, calculated on the basis of the known electron lifetimes in anatase {001} nanoplatelets and in anatase {101} material, was 45 -75 mV upshift for anatase {001}. This expectation is in agreement with the discussed UV-Vis spectroelectrochemical and UPS data. However, in DSSCs assembled for the EIS measurements we observed either zero or insignificant Voc difference. This is inconsistent with our previous observation. But both XPS and UPS are methods not considering electrolyte, solvent, dye and other factors typical for DSSC. Also simplified system (pristine electrode in electrolyte solution) was employed during

UV-Vis spectroelectrochemistry. On the other hand, DSSC is a complex system where many interfaces play role.

The inconsistency in V_{OC} difference (for anatase {001} and anatase {101} photoanodes) observed for DSSCs discussed on the beginning of this section (**Appendix 6**[18]**)** and for DSSCs from EIS measurements (**Appendix 7**[19]**)** could be caused by a difference in electrode assembly too. Deposition of TiO_2 blocking layer and post-treatment in $TiCl_4$ was used during preparation of photoanodes for EIS in contrast to photoanodes used in **Appendix 6**[18] (see Section 3.3). The pastes used for TiO_2 films preparation and loaded dye were different as well (see Sections 3.2 and 3.3). The pure organic dye D35 was used in DSSCs for EIS measurements (**Appendix 7**[19]**)**. On the other hand the organometallic dye C101 with co-adsorbent was used in the DSSCs, where the V_{OC} difference was observed (**Appendix 6**[18]**)**. All these differences in DSSCs composition could have influence on the observed V_{OC} too. Nevertheless, the results concerning flatband potential and number of traps in anatase {001} compared to anatase {101} from mutually independent techniques are consistent.

Besides V_{OC}, the electron lifetime determined from the EIS data is connected also with charge collection efficiency as well as transport time of electrons inside TiO_2 material. We calculated transport time of electrons higher for anatase nanosheets compared to standard anatase nanoparticles, which led to decreased diffusion of electrons in anatase {001} nanosheets. This can be explained by larger number of electron traps too, because of multiple electron-trapping. Despite of lower diffusion coefficient of electrons in anatase {001}, the combination of D_e with longer electron life time led to charge collection efficiency of nanocrystalline anatase {001} similar to that in anatase {101} nanoparticles. In addition the observed longer electron lifetime in anatase {001} nanoplatelets can be a reason for better photocatalytic activity of anatase nanosheets compared to standard anatase nanoparticles.

5. Conclusions

Electrochemical behavior of TiO_2 materials with respect to their applications in Li-ion batteries was investigated. Lithium insertion into anatase nanocrystals with predominant facet {001} and into TiO_2 (B) material was studied electrochemically and compared with Li^+ insertion properties of standard anatase {101} nanoparticles. Analysis of cyclic voltammograms and chronoamperometric data of lithium insertion into anatase {001} nanosheets and into anatase {101} nanocrystals revealed a higher charge capacity, higher diffusion coefficient of Li^+ and lower activation energy of Li^+ insertion for anatase {001} nanoplatelets compared to common anatase {101} nanoparticles. These data indicate facilitated Li^+ transport within anatase {001} nanosheets, and complete previously reported results about Li^+ insertion anisotropy on single-crystal anatase electrodes. The results show anatase {001} nanoplatelets being more active material for Li-ion batteries applications than standard anatase {101} nanoparticles.

Detailed analysis of Li^+ charging mechanism of TiO_2 (B) and TiO_2 anatase {101} was carried out by deconvolution of cyclic voltammograms. The proportion of capacitive processes contribution to the overall current response was determined for both materials. The contribution of capacitive currents to the total current was about 30% higher for TiO_2 (B) than for anatase, even though of 3 times lower surface area of the former. This difference is attributed to the pseudocapacitive Li^+ storage in the open channels of TiO_2 (B) lattice and it is established as a reason of higher electrochemical response of TiO_2 (B) compared to anatase.

Detailed investigation of Li^+ insertion into anatase {101} nanocrystals was made by in situ Raman spectroelectrochemistry employing isotope-labeled compounds $Ti^{16/18}O_2$ and $^{6/7}LiClO_4$. Isotopic shifts in the Raman spectrum of pure orthorhombic Li_xTiO_2 enabled us the assignment of 20 observed vibrational modes. These results help to clarify previous inconsistency in assignment of Raman peaks of orthorhombic lithium titanate to the corresponding vibrations. Moreover, Raman spectroelectrochemistry was found to be a useful technique for detection of trace anatase impurities when XRD, CV or standard Raman spectroscopy are of insufficient sensitivity.

Differences in flatband position and electron energetics of anatase {001} nanosheets and anatase {101} nanoparticles were investigated. A more negative flatband potential was observed

by the UV-Vis spectroelectrochemistry for anatase {001} compared to anatase {101} nanocrystals. These results support previously published data for single crystals. Electrochemical impedance spectroscopy revealed a higher number of electron traps for anatase {001} nanoplatelets than for anatase {101} nanocrystals. This higher amount of electron traps leads to higher transport resistance of electrons in the material and to lower diffusion coefficient. On the other hand, it caused a longer electron lifetime in anatase nanosheets compared to standard anatase nanoparticles.

6. Reference List

1. M. J. Gázquez, J. P. Bolívar, R. Garcia-Tenorio and F. Vaca, *Mater Sci Appl*, 2014, **5**, 441-458.
2. N. Rahimi, R. A. Pax and E. M. Gray, *Prog Solid State Ch*, 2016, **44**, 86-105.
3. L. Kavan, in *Dye-Sensitized Solar Cells*, ed. K. Kalyanasundaram, CRC Press Taylor & Francis, 2010, ch. 2, pp. 45-81.
4. J. F. Banfield and D. R. Veblen, *Am Mineral*, 1991, **76**, 113-127.
5. H. Z. Zhang and J. F. Banfield, *Journal of Physical Chemistry B*, 2000, **104**, 3481-3487.
6. K. R. Zhu, M. S. Zhang, J. M. Hong and Z. Yin, *Mat Sci Eng a-Struct*, 2005, **403**, 87-93.
7. J. Zhang, M. J. Li, Z. C. Feng, J. Chen and C. Li, *Journal of Physical Chemistry B*, 2006, **110**, 927-935.
8. J. W. Wang, A. K. Mishra, Q. Zhao and L. P. Huang, *J Phys D Appl Phys*, 2013, **46**.
9. M. Zukalova, M. Kalbac, L. Kavan, I. Exnar and M. Grätzel, *Chem. Mater*, 2005, **17**, 1248-1255.
10. Y. Q. Zhang, Q. Fu, Q. L. Xu, X. Yan, R. Y. Zhang, Z. D. Guo, F. Du, Y. J. Wei, D. Zhang and G. Chen, *Nanoscale*, 2015, **7**, 12215-12224.
11. J. F. Wang, J. J. Xie, Y. M. Jiang, J. J. Zhang, Y. G. Wang and Z. F. Zhou, *Journal of Materials Science*, 2015, **50**, 6321-6328.
12. L. Sang, Y. Zhao and C. Burda, *Chem. Rev*, 2014, **114**, 9283-9318.
13. X. Chen and S. S. Mao, *Chem Rev*, 2007, **107**, 2891-2959.
14. R. van de Krol, PhD Thesis, Delft University Of Technology, 2000.
15. F. Turci, E. Peira, I. Corazzari, I. Fenoglio, M. Trotta and B. Fubini, *Chem Res Toxicol*, 2013, **26**, 1579-1590.
16. U. Diebold, *Surf. Sci. Rep*, 2003, **48**, 5-229.
17. M. Bousa, B. Laskova, M. Zukalova, J. Prochazka, A. Chou and L. Kavan, *J. Electrochem. Soc*, 2010, **157**, A1108-A1112.
18. B. Laskova, M. Zukalova, L. Kavan, A. Chou, P. Liska, Z. Wei, L. Bin, P. Kubat, E. Ghadiri, J. E. Moser and M. Grätzel, *J. Solid State Electrochem*, 2012, **16**, 2993-3001.
19. B. Laskova, T. Moehl, L. Kavan, M. Zukalova, X. J. Liu, A. Yella, P. Comte, A. Zukal, M. K. Nazeeruddin and M. Graetzel, *Electrochimica Acta*, 2015, **160**, 296-305.

20. H. G. Yang, C. H. Sun, S. Z. Qiao, J. Zou, G. Liu, S. C. Smith, H. M. Cheng and G. Q. Lu, *Nature*, 2008, **453**, 638-642.
21. X. Han, Q. Kuang, M. Jin, Z. Xie and L. Zheng, *J. Am. Chem. Soc*, 2009, **131**, 3152-3153.
22. X. H. Yang, Z. Li, C. H. Sun, H. G. Yang and C. Z. Li, *Chem. Mater*, 2011, **23**, 3486-3494.
23. W. Yang, J. Li, Y. Wang, F. Zhu, W. Shi, F. Wan and D. Xu, *Chem. Commun*, 2011, **47**, 1809-1811.
24. J. G. Yu, L. F. Qi and M. Jaroniec, *J. Phys. Chem. C*, 2010, **114**, 13118-13125.
25. C. L. Olson, J. Nelson and M. S. Islam, *J. Phys. Chem. B*, 2006, **110**, 9995-10001.
26. B. Laskova, M. Zukalova, A. Zukal, M. Bousa and L. Kavan, *Journal of Power Sources*, 2014, **246**, 103-109.
27. R. Marchand, L. Brohan and M. Tournoux, *Mat. Res. Bull*, 1980, **15**, 1129-1133.
28. M. Zukalová, PhD Thesis, Charles University in Prague, 2008.
29. B. Pitna Laskova, L. Kavan, M. Zukalova, K. Mocek and O. Frank, *Monatsh Chem*, 2016, **147**, 951-959.
30. V. Mansfeldova, B. Laskova, H. Krysova, M. Zukalova and L. Kavan, *Catal. Today*, 2014, **230**, 85-90.
31. C. Arrouvel, S. C. Parker and M. S. Islam, *Chem. Mater*, 2009, **21**, 4778-4783.
32. B. Laskova, O. Frank, M. Zukalova, M. Bousa, M. Dracinsky and L. Kavan, *Chem. Mater*, 2013, **25**, 3710-3717.
33. Y. Ren, L. J. Hardwick and P. G. Bruce, *Angew. Chem. Int. Ed*, 2010, **49**, 2570-2574.
34. D. Bresser, E. Paillard, E. Binetti, S. Krueger, M. Striccoli, M. Winter and S. Passerini, *J. Power Sources*, 2012, **206**, 301-309.
35. T. Berger, D. Monllor-Setoca, M. Jankulovska, T. Lana-Villarreal and R. Gomez, *Chemphyschem*, 2012, **13**, 2824-2875.
36. L. Kavan, *Chem. Rec*, 2012, **12**, 131-142.
37. M. Wagemaker, W. J. H. Borghols and F. M. Mulder, *J. Am. Chem. Soc*, 2007, **129**, 4323-4327.
38. W. J. H. Borghols, M. Wagemaker, U. Lafont, E. M. Kelder and F. M. Mulder, *Chem. Mater*, 2008, **20**, 2049.
39. Z. Yang, D. Choi, S. Kerisit, K. M. Rosso, D. Wang, J. Zhang, G. Graff and J. Liu, *J. Power Sources*, 2009, **192**, 588-598.
40. A. R. Armstrong, G. Armstrong, J. Canales and P. G. Bruce, *Angew. Chem. Int. Ed*, 2004, **43**, 2286-2288.
41. A. R. Armstrong, G. Armstrong, J. Canales and P. G. Bruce, *J. Power Sources*, 2005, **146**, 501-506.
42. T. Beuvier, M. Richard-Plouet, M. Mancini-Le Granvalet, T. Brousse, O. Crosnier and L. Brohan, *Inorganic Chemistry*, 2010, **49**, 8457-8464.
43. *Dye-sensitized Solar Cells*, ed. K. Kalyanasundaram, CRC Press Taylor & Francis, 2010.
44. M. Grätzel, *Nature Materials*, 2014, **13**, 838-842.
45. M. Grätzel, *Accounts Chem Res*, 2017, **50**, 487-491.
46. M. Zukalova, B. Pitna Laskova, M. Klementova and L. Kavan, *Electrochimica Acta*, 2017, **245**, 505-511.
47. M. Kitta, K. Kuratani, M. Tabuchi, N. Takeichi, T. Akita, T. Kiyobayashi and M. Kohyama, *Electrochimica Acta*, 2014, **148**, 175-179.
48. Y. Sun, L. Zhao, H. L. Pan, X. Lu, L. Gu, Y. S. Hu, H. Li, M. Armand, Y. Ikuhara, L. Q. Chen and X. J. Huang, *Nat Commun*, 2013, **4**.

49. L. Kavan, M. Kalbac, M. Zukalova, I. Exnar, V. Lorenzen, R. Nesper and M. Grätzel, *Chem. Mater*, 2004, **16**, 477-485.
50. L. Kavan and M. Gratzel, *Electrochem Solid St*, 2002, **5**, A39-A42.
51. L. Kavan, J. Prochazka, T. M. Spitler, M. Kalbac, M. T. Zukalova, T. Drezen and M. Grätzel, *J Electrochem Soc*, 2003, **150**, A1000-A1007.
52. S. Ito, P. Chen, P. Comte, M. K. Nazeeruddin, P. Liska, P. Pechy and M. Grätzel, *Prog. Photovoltaics*, 2007, **15**, 603-612.
53. X. B. Xu, D. K. Huang, K. Cao, M. K. Wang, S. M. Zakeeruddin and M. Grätzel, *Sci. Rep*, 2013, **3**.
54. L. Kavan, T. Stoto, M. Grätzel, D. Fitzmaurice and V. Shklover, *J. Phys. Chem*, 1993, **97**, 9493-9498.
55. G. Redmond and D. Fitzmaurice, *J. Phys. Chem*, 1993, **97**, 1426-1430.
56. G. Rothenberger, D. Fitzmaurice and M. Grätzel, *J. Phys. Chem*, 1992, **96**, 5983-5986.
57. F. Fabregat-Santiago, J. Bisquert, G. Garcia-Belmonte, G. Boschloo and A. Hagfeldt, *Sol. Energy Mater. Sol. Cells*, 2005, **87**, 117-131.
58. R. Hengerer, L. Kavan, P. Krtil and M. Grätzel, *J. Electrochem. Soc*, 2000, **147**, 1467-1472.
59. R. Van de Krol, A. Goossens and J. Schoonman, *J. Phys. Chem. B*, 1999, **103**, 7151-7159.
60. L. Kavan, J. Rathousky, M. Grätzel, V. Shklover and A. Zukal, *J. Phys. Chem. B*, 2000, **104**, 12012-12020.
61. C. W. Mason, I. Yeo, K. Saravanan and P. Balaya, *RSC Advances*, 2013, **3**, 2935-2941.
62. A. G. Dylla, J. A. Lee and K. J. Stevenson, *Langmuir*, 2012, **28**, 2897-2903.
63. J. Wang, J. Polleux, J. Lim and B. Dunn, *J. Phys. Chem. C*, 2007, **111**, 14925-14931.
64. T. Brezesinski, J. Wang, J. Polleux, B. Dunn and S. H. Tolbert, *J. Am. Chem. Soc*, 2009, **131**, 1802-1809.
65. K. Zhu, Q. Wang, J. H. Kim, A. A. Pesaran and A. J. Frank, *J. Phys. Chem. C*, 2012, **116**, 11895-11899.
66. N. N. Dinh, N. T. T. Oanh, P. D. Long, M. C. Bernard and A. Hugot-Le Goff, *Thin Solid Films*, 2003, **423**, 70-76.
67. R. Baddour-Hadjean, S. Bach, M. Smirnov and J. P. Pereira-Ramos, *J. Raman Spectrosc*, 2004, **35**, 577-585.
68. L. J. Hardwick, M. Holzapfel, P. Novák, L. Dupont and E. Baudrin, *Electrochim. Acta*, 2007, **52**, 5357-5367.
69. O. Frank, M. Zukalova, B. Laskova, J. Kurti, J. Koltai and L. Kavan, *Phys Chem Chem Phys*, 2012, **14**, 14567-14572.
70. L. Kavan, M. Zukalova, M. Ferus, J. Kürti, J. Koltai and S. Civis, *Phys. Chem. Chem. Phys*, 2011, **13**, 11583-11586.
71. B. Elgh and A. E. C. Palmqvist, *Journal of Sol-Gel Science and Technology*, 2015, **76**, 395-401.
72. J. Zhang, P. L. Liu, Z. D. Lu, G. L. Xu, X. Y. Wang, L. S. Qian, H. B. Wang, E. P. Zhang, J. H. Xi and Z. G. Ji, *Journal of Alloys and Compounds*, 2015, **632**, 133-139.

7. List of Appendices

Appendix 1: Milan Bousa, Barbora Laskova, Marketa Zukalova, Jan Prochazka, Alison Chou and Ladislav Kavan. "Polycrystalline TiO_2 Anatase with a Large Proportion of Crystal Facets (001): Lithium Insertion Electrochemistry." *J. Electrochem. Soc*, 2010, **157**, A1108-A1112.

Appendix 2: Barbora Laskova, Marketa Zukalova, Arnost Zukal, Milan Bousa and Ladislav Kavan. "Capacitive Contribution to Li-storage in TiO_2 (B) and TiO_2 (anatase)." *Journal of Power Sources*, 2014, **246**, 103-109.

Appendix 3: Barbora Laskova, Otakar Frank, Marketa Zukalova, Milan Bousa, Martin Dracinsky and Ladislav Kavan. " Lithium Insertion into Titanium Dioxide (Anatase): A Raman Study with $^{16/18}O$ and $^{6/7}Li$ Isotope Labeling." *Chem. Mater*, 2013, **25**, 3710-3717.

Appendix 4: Barbora Pitna Laskova, Ladislav Kavan, Marketa Zukalova, Karel Mocek and Otakar Frank. "In situ Raman spectroelectrochemistry as a useful tool for detection of TiO_2(anatase) impurities in TiO_2 (B) and TiO_2 (rutile)." *Monatsh Chem*, 2016, **147**, 951-959.

Appendix 5: Markéta Zukalová, Barbora Pitňa Lásková, Mariana Klementová and Ladislav Kavan. "Na insertion into nanocrystalline $Li_4Ti_5O_{12}$ spinel: An electrochemical study." *Electrochim. Acta*, 2017, **245**, 505-511.

Appendix 6: Barbora Laskova, Marketa Zukalova, Ladislav Kavan, Alison Chou, Paul Liska, Zhang Wei, Liu Bin, Pavel Kubat, Elham Ghadiri, Jacques E. Moser and Michael Grätzel. "Voltage enhancement in dye-sensitized solar cell using (001)-oriented anatase TiO_2 nanosheets." *J. Solid State Electrochem*, 2012, **16**, 2993-3001.

Appendix 7: Barbora Laskova, Thomas Moehl, Ladislav Kavan, Marketa Zukalova, Xianjie Liu, Aswani Yella, Pascal Comte, Arnost Zukal, Mohammad Khaja Nazeeruddin and Michael Graetzel. "Electron Kinetics in Dye Sensitized Solar Cells Employing Anatase with (101) and (001) Facets." *Electrochim. Acta*, 2015, **160**, 296-305.